UNIVERSIDADE FEDERAL DO CEARÁ
CENTRO DE CIÊNCIAS
DEPARTAMENTO DE FÍSICA
BACHARELADO EM FÍSICA

JOHNATHAS D'ARF SEVERO FORTE

DIRAC CONES IN GATED MULTILAYER BLACK PHOSPHORUS

FORTALEZA
2018

JOHNATHAS D'ARF SEVERO FORTE

DIRAC CONES IN GATED MULTILAYER BLACK PHOSPHORUS

Monografia de Bacharelado apresentada à Coordenação de Graduação do Curso de Física, da Universidade Federal do Ceará, como requisito parcial para a obtenção do Título de Bacharel em Física.

Orientador: Prof. Dr. Andrey Chaves
Orientador: Dr. Duarte José Pereira de Sousa

FORTALEZA
2018

Dados Internacionais de Catalogação na Publicação
Universidade Federal do Ceará
Biblioteca Universitária
Gerada automaticamente pelo módulo Catalog, mediante os dados fornecidos pelo(a) autor(a)

F841d Forte, Johnathas D'arf Severo.
Dirac Cones in Gated Multilayer Black Phosphorus / Johnathas D'arf Severo Forte. – 2018.
67 f. : il. color.

Trabalho de Conclusão de Curso (graduação) – Universidade Federal do Ceará, Centro de Ciências, Curso de Física, Fortaleza, 2018.
Orientação: Prof. Dr. Andrey Chaves.
Coorientação: Prof. Dr. Duarte José Pereira de Sousa.

1. Semicondutores. 2. Fosforeno. 3. Dirac. 4. Materiais 2D. I. Título.

CDD 530

JOHNATHAS D'ARF SEVERO FORTE

DIRAC CONES IN GATED MULTILAYER BLACK PHOSPHORUS

Monografia de Bacharelado apresentada à Coordenação de Graduação do Curso de Física, da Universidade Federal do Ceará, como requisito parcial para a obtenção do Título de Bacharel em Física.

Orientador: Prof. Dr. Andrey Chaves
Orientador: Dr. Duarte José Pereira de Sousa

Aprovada em: 03/12/2018.

BANCA EXAMINADORA

Prof. Dr. Andrey Chaves (Orientador)
Departamento de Física – UFC

Prof. Dr. João Milton Pereira Jr.
Departamento de Física – UFC

Prof. Dr. Jeanlex Soares de Sousa
Departamento de Física – UFC

Dedicated to Mom.

AKNOWLEDGEMENTS

I wish to express my gratitude to a number of people and institutions that contributed directly and indirectly to the completion of the present work.

To Dr. Duarte J. P. de Sousa, for his mentorship, guidance and, most importantly, friendship. The suggestion of the topic of this Monograph came from him and he directly helped me with a number of calculations presented here. To Prof. Andrey Chaves for his enormous patience, availability and his always caring attitude towards his (and anyone's) students. To Prof. J. Milton P. Jr. and Prof. Jeanlex S. de Sousa for the useful discussions which helped towards the completion of this work, and also for participating in my Examination Board, as well as for trying to get me a Iniciação Científica (IC) scholarship. To all Professors from the Physics Department whom I've learned a great deal from during classes and conversations, in particular, Profs. J. Afonso (Mathematics Department), Gil de Aquino, Josué Mendes Filho, R. V. Maluf, J. Ramos, R. Renan and Saulo D. S. Reis. To Prof. Tony Low from University of Minnesota for providing valuable insight on how to include screening effects in the tight-binding calculation. To Profs. Nildo and Marcos Antônio for maintaining the *Monitoria da Física* project, which helped to financially support me during the present year.

To my friends from University and from GTMC, in particular, Gabriel, Levi, Luan and Lucas for the support, companionship and love. Without them, returning to UFC and remaining here would have been incredibly more difficult. To Daniel, Diego, Israel (Koala), João, Kaique, Lucas Moreira, Mardônio and Pablo for all the studying and time spent together in the last year of University. To the many friends I made online which helped me endure very difficult years, in particular, Albert, Amanda, Cecily, Cindy (Kiddo), Cyd, Diego (Kuma), Freddie (Combo), João (Fanta), Koenraad (Viri), Leah, Rodrigo, Sani and everyone from *Synchrony/Dark Side*. To Larissa, for always being there. To every one from my CEFET (now IFCE) classmates, in particular, Jonas, Rustênio, David and Ercílio who made studying there even more fun than it already was. To my old friends Haroldo, Nathália, Jonny, Marcus and Sofia, for sticking around for so long. To Osvaldo, for his apparently limitless generosity. To Lucas (again), Ramon, Iago and João Pedro for all the good times and for helping to make church music more *interesting*.

To all employees of Universidade Federal do Ceará, from the cleaning personnel to the bus drivers, for everything they do to maintain and support the student life in the University. To Luíza and Soraia from PRAE (*Pró-Reitoria de Assuntos Estudantis*) for their therapeutical services. To everyone from *Cantina da Química*, for the coffee.

To Richard Feynman, Frank Zappa and Pink Floyd for the endless source of inspiration.

To my family, especially Tia Sinhá, Tia Elinalva, Tia Eroniza, Tio Geraldo and my cousins João Paulo, Jordano and Marden for the fun, care, love and support they provided during my entire life. To Gabi, for the food, movies, love, care and support during the hardest and also the happiest times, as well as for having the cutest cat ever. To Zack, the dog.

To Mom for... everything, really. To Dad — I wish you were here.

"What I cannot create, I do not understand."

Richard P. Feynman

Resumo

Fósforo negro, uma das formas alotrópicas do elemento fósforo, tem recebido bastante atenção desde a sua redescoberta, em 2014, da perspectiva de um material bidimensional. Devido às suas propriedades interessantes, tais como alta mobilidade de portadores de carga e seu *gap* de energia que depende da espessura, o fósforo negro é considerado um material com grande potencial para aplicações em nano e optoeletrônica. Em particular, o intervalo de valores que seu gap de energia pode assumir, variando de $\sim$ 2 eV (monocamada) até $\sim$ 0.3 eV(*bulk*), é de grande importância, já que ele cobre uma porção do espectro eletromagnético que não é alcançada por nenhum outro semicondutor bidimensional. Além disso, o gap de energia também pode ser regulado de outras maneiras, como através da aplicação de um campo elétrico externo perpendicular. Foi demonstrado que esse mecânismo induz uma transição de fase topológica no sistema, transformando o fosforeno de um semicondutor em um semimetal e, eventualmente, em um semimetal de Dirac, quando é observada a presença de cones de Dirac no espectro de energia do material.

Nessa Monografia, nós exploramos as propriedades eletrônicas do fosforeno no contexto do modelo da ligação forte (*tight-binding*), usando uma aproximação de um campo elétrico sem blindagem, dando ênfase ao surgimento de cones de Dirac, uma transição que ocorre quando a densidade eletrônica em um dos *gates* n_g, associada com o campo elétrico externo, é maior do que um valor crítico n_c. Após isso, um cálculo semelhante é feito para nanofitas de fosforeno com bordas *zigzag* e *armchair*. Por fim, sugerimos um método para estimar a espessura e a orientação das bordas de nanofitas de fosforeno.

Abstract

Black Phosphorus, one of the allotropes of the element Phosphorus, has gained a lot of attention since its rediscovery from the perspective of a two-dimensional material in 2014. Due to its interesting properties, such as high carrier mobility and thickness-dependent energy gap, multilayer BP is considered a material with great potential for applications in nano and optoelectronics. In particular, the wide range of values that its thickness-dependent gap can assume, ranging from ~ 2.0 eV (single-layer) to ~ 0.3 eV (bulk), has significant importance since it covers a broad range of the electromagnetic spectrum, not reached by other two-dimensional semiconductors. Additionally, the gap can also be tuned by other means, such as the application of an external perpendicular electric field. It has been shown that such mechanism induces a topological phase transition in the system, turning phosphorene from a semiconductor into a semi-metal and eventually into a Dirac semi-metal, at which stage the presence of Dirac cones can be observed in the energy spectrum of phosphorene.

In this Monograph, we explore the electronic properties of gated multilayer phosphorene within the context of a tight-binding model, using an unscreened electric field approximation, giving emphasis to the appearance of the Dirac spectra, a transition that occurs when the gate density n_g associated with the external electric field is greater than some critical value n_c. Afterwards, a similar calculation is performed for phosphorene nanoribbons with zigzag and armchair edges. Finally, we suggest a scheme to determine the thickness and edge orientation of phosphorene nanoribbons.

CONTENTS

1 BLACK PHOSPHORUS: A BRIEF OVERVIEW

1.1 General Introduction

Black Phosphorus (BP) is the most stable allotrope of the element Phosphorus [1]. It was first successfully synthesized in 1914 by Pierce Williams Bridgman by exposing white phosphorus to temperatures as high as 200°C and to pressures over 1 GPa [2]. Research on this material remained relatively silent for about 100 years, especially in the context of electronics, since the attention has been directed mostly towards Silicon, Germanium and other types of semiconducting materials [3]. However, in 2014, BP was rediscovered from the perspective of a two dimensional (2D) material. The reason for the growth in interest was twofold. First, with the isolation of graphene in 2004, it was confirmed that 2D sheets of atoms are physically realizable, in opposition with the prevailing theories of Peierls and Landau [4, 5]. This discovery ignited research for new materials that could also exist in a 2D form. After graphene, it was predicted that transition metal dicalchogenides (TMDs) could also exist in 2D, which was readily confirmed in the following years. Second, the low dimensionality and richness in properties that are useful for technological applications matched the search for new materials that can potentially substitute conventional semiconductors as they reach their miniaturization limit.

BP has demonstrated to be an equally promising material for scientific exploration and, in some respects, even more promising than its 2D counterparts for technological applications. Therefore, in this chapter, we discuss some of the general properties of BP, such as it's crystalline and electronic structure; discuss methods of synthesis and, finally, discuss briefly the intriguing topological phase transition that occurs in BP under some specified conditions. The latter is closely related to the main topic of this Monograph.

1.2 Atomic and Band Structures

1.2.1 Crystalline Structure

The electronic configuration of the ground state phosphorus atom is $1s^2\ 2s^2\ 2p^6\ 3s^2\ 3p^3$. In order to meet the octet requirement, it needs three more electrons in the valence shell. In all allotropic forms of phosphorus, a P atom is bonded to three other atoms in order to meet this requirement. In white phosphorus, for instance, the P atoms are bonded together in a tetrahedral unit containing four atoms with six bonds. Such a geometry does not allow for structurally stable bonds, since the $3p$ orbitals which they stem from cannot adopt the angles that they normally would. Therefore, this allotrope is quite unstable. In BP, on the other hand,

three of the bonds are broken to form sp^3 bonds resulting in the double layered structure of BP with bond angles of 96.34°and 102.09°, which are much closer to a perfect tetragonal structure. This results in the increased stability of the crystal [28]. This structure was first confirmed by Hultgren *et al* in 1935 using a x-ray detection method. The individual layers of BP, unlike those of graphite (where the bonds stem from sp^2 hybrid orbitals) form a puckered structure, represented in Figs. 1 (a) and (b). Much like graphite, however, the individual layers of BP are held together by weak van der Waals forces and the nature of the interlayer strength is what allows the material to be mechanically exfoliated. The atomic structure of BP has been probed by means of scanning transmission electron microscopy (STEM) [13]. The images show the arrangement of the phosphorus atoms inside each layer and also their stacking order, as seen in Fig. 1 (c).

[h]

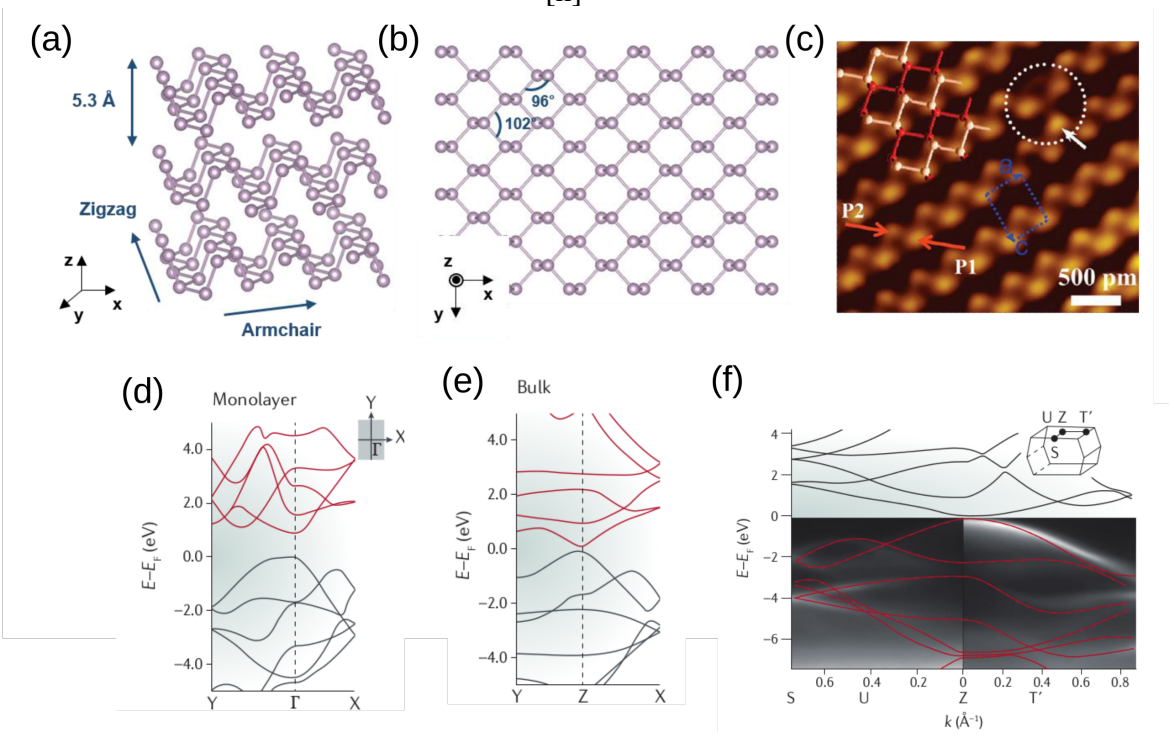

Figure 1: (a,b) Schematic view of the crystalline structure of BP, highlighting the zigzag and armchair directions, interlayer distance and in-plane bonding angles. (c) Close-up showing scanning tunneling microscope (STM) image of upper atoms of the topmost layer of BP. A puckered structure can be seen. The band structure calculated from DFT for (d) monolayer and (e) bulk show clearly the direct gap at the Γ point. In (f) one can see the occupied valence obtained from ARPES measurements in comparison with the full band structure obtained from first-principles calculations for bulk BP. The gap is located at the Z point of the Brillouin zone, which is directly above the Γ point. Figure adapted from Refs. [13, 14, 28]

1.2.2 Band Structure

BP is a direct gap semiconductor. Unlike other 2D materials, the gap remains direct from bulk all the way down to a single-layer. A direct band gap is a very attractive feature for

optoelectronic applications since electrons can be excited from the top of the valence band to the conduction band without having to interact with a phonon to gain the required momentum. The band gap in BP has been calculated theoretically and measured experimentally to vary with the number of stacked layers, from ≈ 0.3 eV (bulk) to ≈ 2 eV (monolayer), as can be seen in Fig.1 (a) and Figs. 1(d) and (e) [8, 22, 12]. This increase in the band gap value with a decreasing number of layers can be explained due to the quantum confinementt in the z direction. Besides varying the number of layers, the gap can also be tuned via other mechanisms such as the application of mechanical strain and perpendicular electric fields via gating and/or doping.

As a direct consequence of its crystalline strucutre, the band structure of phosphorene is highly anisotropic. Interesting effects arise from such anisotropy, such as different effective masses for electrons and holes in different directions [28, 62]. Heat conduction, carrier mobility and optical properties also vary in different directions [14]. If confinement takes place in the plane of the layers, as in the case of armchair and zigzag nanoribbons, the gap scales differently with the width depending on the edge type, going as $1/W$ for zz edges and $1/W^2$ for armchair edges [61].

Under different mechanisms, the band structure of BP undergoes a phase transition that changes the material from a normal semiconductor to a Dirac semimetal. This intriguing property will be explored in a later section.

1.3 Anisotropy beyond the band structure

1.3.1 Mechanical properties

Due to the weak van der Waals interactions in the z direction and the strong in-plane covalent bonds, phosphorene responds differently to compression and stress in different directions. For instance, Guan *et al* [15] found, in a theoretical study, that, when subjected to compressive and tensile in-layer strain up to 2%, the change in interlayer distance was different for different directions of applied forces. By compressing the crystal along the x direction, the interlayer distance increased. On the other hand, both compression and stretching in the y direction causes the interlayer distance to decrease, revealing the anisotropy of the crystal and a negative Poisson ratio between the z and the y directions [15]. The DFT calculations from Wei *et al* [16] found direction-dependent critical tensile strain for monolayer BP with the values of 27% and 30% for the y and x directions, respectively. They also found the critical tensile strain for a bilayer system to be the increase to 32% in the X direction and decrease to 24% in the y direction. These values remain constant for an increasing number of layers [16]. Other studies found that bond angles and the band structure change differently for strain applied in different directions [54, 55].

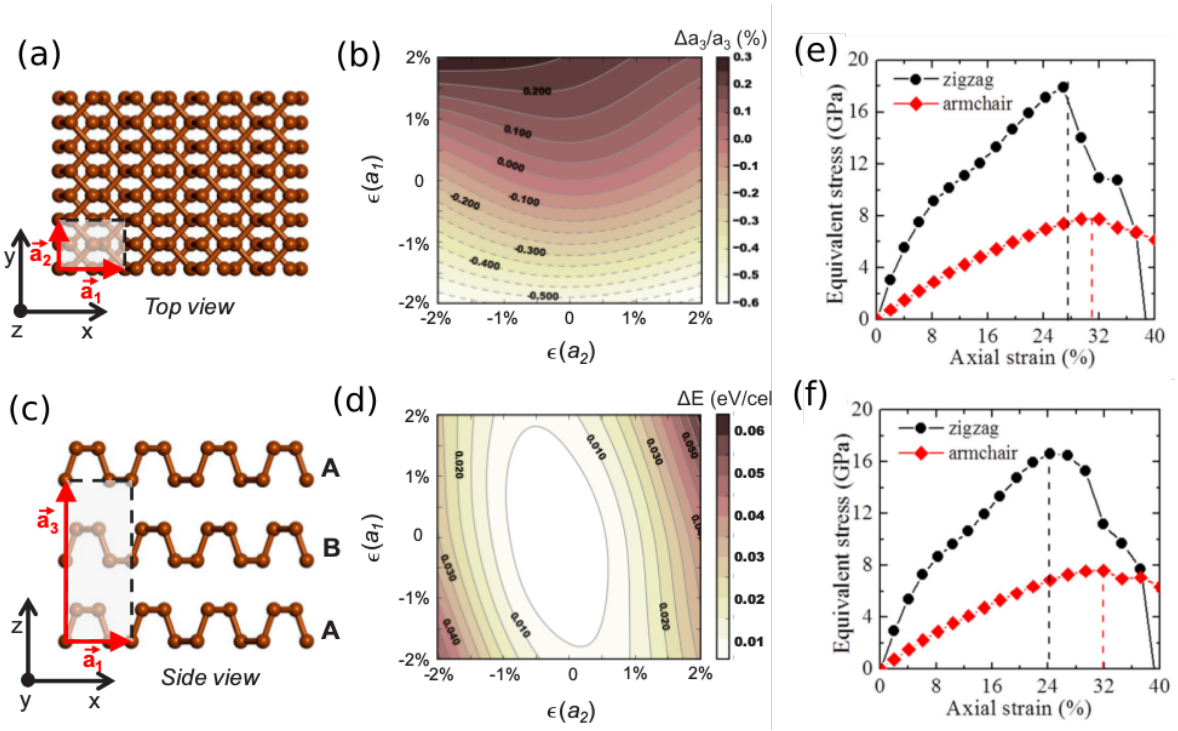

Figure 2: (a) Top-view model of the BP crystalline structure. (b) Fractional change of interlayer distance a_3 as a function of the in-layer strain ϵ along the $\vec{a_1}$ and $\vec{a_2}$ directions. The strain-stress relation for (e) monolayer and (f) two-layer phosphorene structures. The critical strains for monolayer are 27% (zigzag) and 30% (armchair), whereas the critical strains for multilayer BP are 24% (zigzag) and 32% (armchair). Figures adapted from Refs. [15, 16].

1.3.2 Optical Properties

As a result of its anisotropy, BP possesses linear dichroism (light rays with different polarizations are absorbed at different rates) [19, 20, 21]. For a dielectric polarization in the armchair direction, the band edge of the first absorption peak was found at the band gap (around 1.55 eV in this particular study, for the monolayer) and therefore decreased rapidly with the thickness. In contrast, with light polarized in the zigzag direction the first absorption peak was found at 3.14 eV for the monolayer and its position shifted very slowly with increasing thickness, remaining at 2.76 eV in bulk. Another study explained the linear dichroism for bulk BP with an analysis of the optical selection rules [21]. Since only the zigzag direction has mirror relection and inversion symmetries, electronic states at high symmetry points in the Brillouin zone, such as the points Z and Γ, can be labelled by these two symmetries. Each of the symmetries results in an optical selection rule. The first selection rule is associated with the parity of the photons while the second concerns the polarization of normal incident light. Since photons carry parity -1, optical absorption can only occur between states with opposite parities. Under mirror reflection, the in-plane components of the electric and magnetic field (E_x, E_y, B_x, B_y) shift differently for light polarized in different directions. For light polarized in the y direction, the components change sign $(E_x \to -E_x, B_x \to -B_x)$, whereas for light

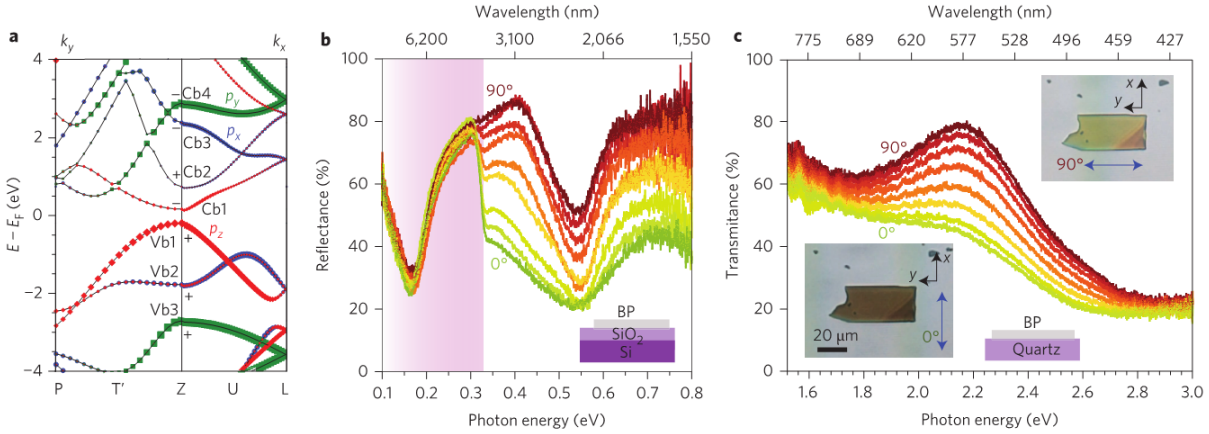

Figure 3: Optical selection rules and broadband linear dichroism in BP. (a) Orbital component analysis of bulk BP band dispersion. The "+" and "−" signs represent the parity of the bands. (b) Light polarization dependence of reflection in the infrared spectral regime, showing around 50% variation in reflection along two perpendicular directions for energies above the bandgap (purple shaded area). (c) Polarization dependence of the transmission of visible light. In (b) and (c) the incident light is linearly polarized in directions ranging from the x to the y in 15°steps. Figure extracted from Ref. [21]

polarized in the x direction, the signs remain unchanged ($E_x \rightarrow E_x, B_x \rightarrow B_x$).

A theoretical investigation of the angle dependence of light absorption was carried out by Low *et al* using first-principles calculations in conjunction with the $\mathbf{k} \cdot \mathbf{p}$ approximation [22]. It was observed that the absorption coefficient exhibited a strong dependence on the polarization angle. Furthermore, the absorption anisotropy was found to be rather sensitive to the inter-band coupling, evolving from a "dumbbell" shape to one resembling that of an ellipse. The obtained results and a comparison with infrared spectroscopy measurements for a 40 nm film are shown as a polar representation in the Figs. 4 (a) and (b).

Photoluminescence excitation spectroscopy experiments performed by Wang *et al* on monolayer BP reported highly anisotropic and tightly bound excitons. The binding energy was measured to be around 0.9 ± 0.12 eV, which are in agreement with theoretical calculations [24, 25]. Such high exciton binding energies are expected in single-layer semiconductors due to reduced dimensionality and reduced screening of the Coulomb interaction. Polarization-resolved photoluminescence of a monolayer sample (with excitation polarization and detection oriented selectively along either the x or y axes) showed a peak with a full-width at half-maximum of $\sim$ 150 meV centered at $\sim$ 1.3 eV. Their findings reveal that the highest photoluminescence intensity happens when both excitation and detection polarizations are set along the x direction. The emission along the y direction is consistently less than 3% of that along the x direction. Such findings are consistent with previous first-principles simulations [23, 26].

Finally, the band gap of BP covers an electromagnetic spectrum range wider than any other known 2D material to date, which is another indication of its potential in optoelectronics. With graphene operating in the $0 - 0.2$ eV range and most TMDs operating in the 1.0 -

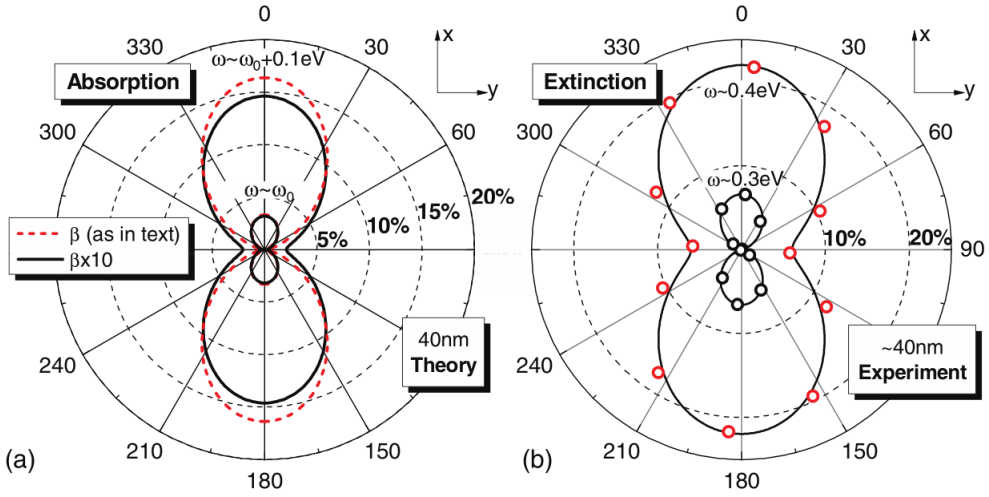

Figure 4: (a) Polar representation of the absorption coefficient for a 40 nm intrinsic BP film for normal incident light with excitation energies at the band gap ω_0 and larger. α is the polarization angle. The absorption coefficient is plotted for two values of interband coupling strenghts. (b) Polar representation of the experimental extinction spectra obtained from infrared spectroscopy for a $\sim$ 40 nm BP film on a SiO_2 substrate. Figure extracted from Ref. [22].

2.0 eV range, BP (0.3 - 2.0 eV) effectively bridges the gap between the two existing classes of 2D materials, operating in the mid-infrared, near-infrared and visible frequency range [3].

1.3.3 Transport Properties

One of the first experimental studies to report the realization of single-layer and few-layer BP also detected anisotropic carrier transport properties [9]. A BP sample with the thickness of $\sim$ 10 nm was obtained by mechanical exfoliation and transferred onto a $\sim$ 90 nm thick SiO_2 substrate. Metal contacts of Ti/Au were defined symmetrically around the sample with a fixed angular interval of 45°. The four diametrically opposed pairs of contacts were used as source/drain for a transistor geometry in order to measure the transistor properties of each device. The system is represented in Fig.5 (a). It was observed a clear angle dependence of the gate current and also of the transconductance, as shown in Fig.5 (b). The anisotropic behaviour is approximately sinusoidal, with minima of drain current at 45 and 225°and maxima at 135 and 315°. The hallmark of anisotropic transport properties in this experiment are the different values of drain current at orthogonal directions. Such results can be partially explained with the band structure of BP, which was calculated from first-principles in this study as seen in Fig. 5(c). The carrier transport along the X direction corresponded to the $\Gamma - Y$ direction with effective mass of $m_e \approx m_h = 0.3m_0$, whereas carrier transport in the Y direction corresponded to transport along the $\Gamma - X$ direction with effective masses of $m_e = 2.6m_0$ and $m_h = 8.3m_o$. A theoretical investigation of the anisotropic carrier properties of single-layer, few-layer and bulk BP was made by Qiao *et al* in 2014 using DFT. This study found that regardless of the type of carrier, their mobility was consistently different in the X and Y directions. The effective

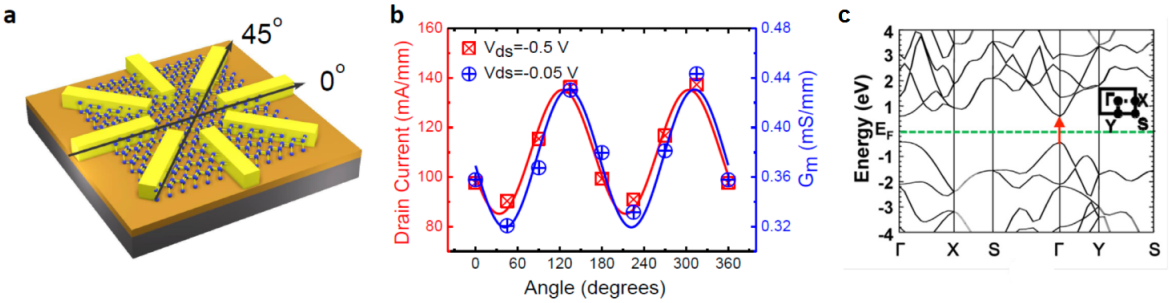

Figure 5: (a) Device structure used to determine the angle-dependent transport behavior. Zero degree is defined by the electrodes, not a few-layer phosphorene crystal orientation. (b) Angular dependence of the drain current and the transconductance G_m of a device with a film thickness of $\sim$ 10 nm. Figure extracted from Ref. [9]

masses of electrons and holes were also found to differ from one another with an increasing number of layers. First-principles calculations performed by Fei *et al* [54] discovered that, by applying appropriate uniaxial (less than 6%) or biaxial strain (less than 4%), the anisotropy of the electron effective mass can be rotated by 90% in-plane, while the anisotropy of holes is not perturbed at all.

1.4 Synthesis and Challenges

1.4.1 First syntheses of bulk BP

Bridgman's attempt to transform white phosphorus into red phosphorus resulted in the first discovery of BP [2]. The white phosphorus was melted under water into a steel shell and then put under kerosene in a high pressure cylinder immediately, after water was removed by mechanical shaking. Pressures up to 0.6 GPa were applied to the sample in a cylinder, which was then raised to 200°C, with a successive increase of pressure up to $\sim$ 1.2 GPa. The transition to BP thus occurred in 5 to 30 minutes. The density of this new allotropic form of phosphorus (2.691 g cm^{-3})was found to be at least 15% higher than the most dense version of red phosphorus found at the time (2.34 g cm^{-3}). Thermoelectrical measurements showed that BP became more conductive with increasing temperature, in constrast with white and red phosphorus, which were known to be insulators. Bridgman reasoned that the higher density of BP would explain this: since BP had a more tightly arranged atomic structure, this would squeeze out electrons from the atoms so that they could move freely with the application of an electric field. This explanation was, of course, previous to the advent of quantum mechanics. A quantum mechanical explanation of the conductivity properties of BP relies heavily on the existence of band structure and how the bands are filled according to Pauli's exclusion principle. Later on he obtained BP from red phosphorus at the even higher pressures of 8 GPa at room temperature [27].

In 1953, Robert W. Keyes improved on Bridgman's method by providing an ability

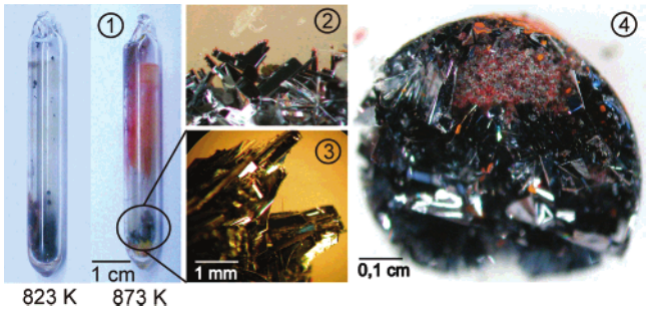

Figure 6: Silica ampoles (picture 1) used for the preparation of BP (picture 3). Sn(IV) iodide condensed on top of BP after thermal decompositon (picture 2). Representative batch of BP grown on top of Au_3SnP_7/AuSn bulk (picture 4). Figure extracted from Ref. [32]

to control the crystallinity of the sample [28, 29]. It also demonstrated by Brown and Rundqvist that BP in small, needle-shaped crystals could be obtained from a white phosphorus solution in liquid bismuth as residue, after dissolving the bismuth matrix in nitric acid [30]. This method went by the name of bismuth-flux method, which was improved upon in 1989 by Baba *et al* [31]. In 2007, yet another way to obtain crystalline BP was found by Lange *et al*. The process yielded samples with good crystallinity from red phosphorus at low pressures at 873 K by adding small quantities of gold, tin and tin (IV) iodide. One of the major downsides of this method was the long time it took to be concluded, ranging from 10 to 70 hours [32].

1.4.2 Phosphorene: 2D BP

In 2014, a number of papers were published reporting the theoretical and experimental rediscovery of BP from the perspective of a 2D semiconductor [8, 33, 9, 34, 11, 19]. Similarly to other layered materials, it was first obtained in this form via micromechanical exfoliation. Although this method is capable of yielding high-quality single-layer and few-layer phosphorene crystals, it is not suited for large-scale production, which limits its use for a wide range of applications. Methods that have been utilized to fabricate other few-layer materials have been applied successfully to BP, such as chemical vapor deposition (CVD), plasma etching (PE) and liquid phase exfoliation (LPE).

In CVD, a solid material is deposited from a vapor by a chemical reaction occurring on or in the vicinity of a normally heated substrate surface [36], producing solid material in the form of a thin film, powder, or single crystal. This procedured has been used to obtain thin films of phosphorene with average areas of $> 3\mu$m and thicknesses representing samples with approximately four layers and of $> 100\mu$m for even thicker samples [37]. The inevitable presence of defects in current CVD-grown samples and the time-consuming process of characterizing them is one of the major downsides of this method [38].

In PE, a high-speed stream of plasma of a suitable gas mixture is shot in pulses at the sample. What follows is the embedding of the atoms of the shot element at or just

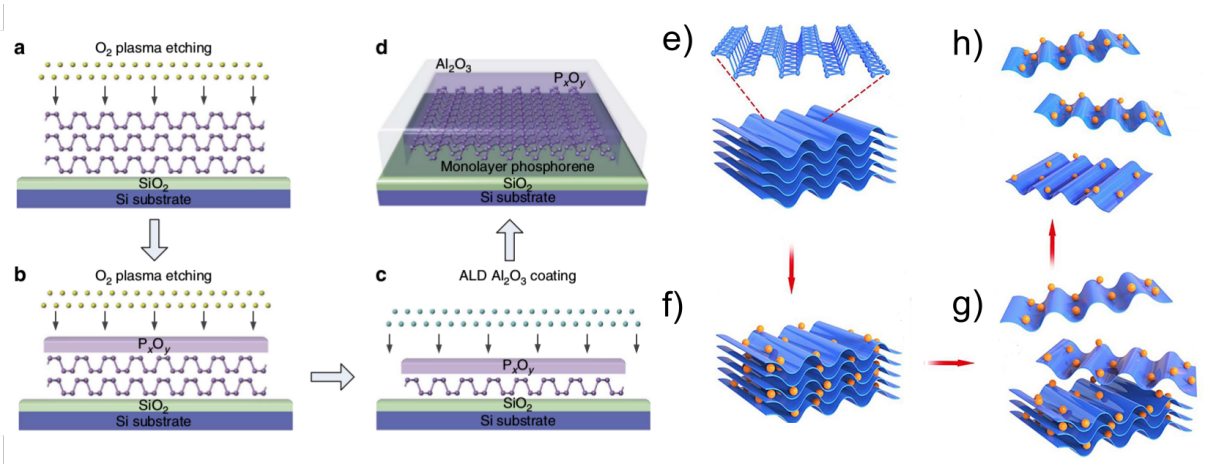

Figure 7: Scheme of the fabrication of phosphorene by PE. (a) A thick BP flake is exfoliated onto a SiO_2 substrate and the sample is treated with O_2 PE. (b) and (c) Oxydation of the topmost phosphorene layers transforming into P_xO_y. Continued etching reduces the number of layers, thinning the material to any number of layers as desired. (d) Al_2O_3 coating of the sample to further improve its lifetime. (e)-(h) A scheme of the solvothermal process used to obtain nanosheets of BP. Figure adapted from Refs. [39, 45].

below the surface of the target by means of chemical reactions. Few-layer and single-layer BP samples were obtained by O_2 PE. In this process, O_2 plasma was shot onto mechanically exfoliated thick BP samples on a SiO_2 substrate. The top layers of the phosphorene flake were oxydized becoming P_xO_y, which served as a protective layer for the remaining phosphorene sample underneath. Further etching can penetrate the P_xO_y and oxydize the deeper layers, reducing the phosphorene sample down to few- and even single-layer. The degradation of the remaining layers is inhibited due to the protective P_xO_y layers [39]. The upside of this method is the air-stable phosphorene produced and the high controllability of the process. However, it still depends upon exfoliation of thick BP crystals.

The most promising way to produce nanosheets in larger quantities is by LPE [40]. This method consists roughly of immersing a layered material into a liquid that will contribute to the weakening of the interlayer forces that hold the material together. Some other process, such as (sonication, shearing or mechanical shaking), is then used to complete the separation of the layers. Although phosphorene was successfully obtained by this method [41, 42], it can be problematic due to the unstability of phosphorene when exposed to humidity, degrading via reactions with water and oxygen. Therefore, efforts have been drawn in the direction of stabilizing liquid exfoliated BP nanosheets against oxidation. Hanlon *et al* performed liquid phase exfoliation using N-cyclohexyl-2-pyrroidone (CHP) as a solvent and obtained relatively stable BP nanosheets by having the solvation shell acting as a barrier against the action of the oxydant species [43]. More recently, Bat-Erdene *et al* used microwave(MW)-assisted liquid phase exfoliation to obtain high-quality, protected against degradation few-layer BP using organic solvents, reducing the processing time from many hours to a few minutes [44]. The lateral

dimensions of their sample was measured to range from hundreds of nanometers to ~ 4 μm with a thickness of less than 10 nm. Liu *et al* used a solvothermal-assisted liquid exfoliation to obtain large size and high quality BP nanosheets using high-polar acetonitrile (ACN) solvent. The solvothermal process weakens the van der Waals forces between the BP layers. After that, ultrasonic processing completes the exfoliation [45]. Atomic force microscopy, transmission electron microscopy and Raman spectroscopy results showed that the samples were less than 2 nm thick while being up to ~ 10 μm wide.

1.4.3 Stability and Passivation Techniques

Due to their high surface area, layered 2D materials possess enhanced chemical reactivity and are thus susceptible to degradation when exposed to an ambient environment [46]. The process was first observed by Yau *et al* using STM surface imaging experiments [47]. After that, a number of studies were performed using more comprehensive techniques, including one by Gamage *et al*, which used nanoscale time series imaging over the course of several months [48]. Their results are shown in Figure 8. Small bubbles start to appear slowly and, as time goes on, they proliferate more rapidly on the surface of the material, eventually reaching a saturation point. Such oxidation bubbles can be detected experimentally by means of Raman spectroscopy. The peaks of the Raman spectra become increasingly smaller, since the bubbles to not contribute to it [49].

Efforts have been drawn towards understanding the mechanisms which cause BP's degradation in ambient conditions. *In situ* Raman spectroscopy and TEM have been used to establish that the rate of oxidation of BP depends strongly on the concentration of oxygen, intensity of light and the energy gap (therefore, the number of layers) [49]. Another experimental investigation on BP's oxidation was made under controlled oxidative environment, consisting of different ratios of O_2 and H_2O using x-ray electron microscopy. They concluded that BP oxidation is likely to be caused by a mutual effect of water and oxygen, where water drives the oxidation via the reaction with the surface oxide which then creates oxygen dissociations.

A number of methods have been proposed to protect BP from oxidation. In general, they come down to coatings (inorganic and hybrid organic-inorganic) and surface functionalization [50]. The former consists of introducing a physical barrier that prevents the BP from being oxydized, such as the O_2 plasma etching process described earlier. As mentioned previously, the solvation shell produced in the solvothermal LPE process described earlier works as a protecting barrier, preventing the nanosheets from reacting with oxygen and water. The coating agent can also bond to the lone pairs of electrons and make BP less reactive. A double-layer capping of Al_2O_3 and hydrophobic fluoropolymer was demonstrated to make BP more stable, serving as an example of hybrid organic-inorganic coating [50].

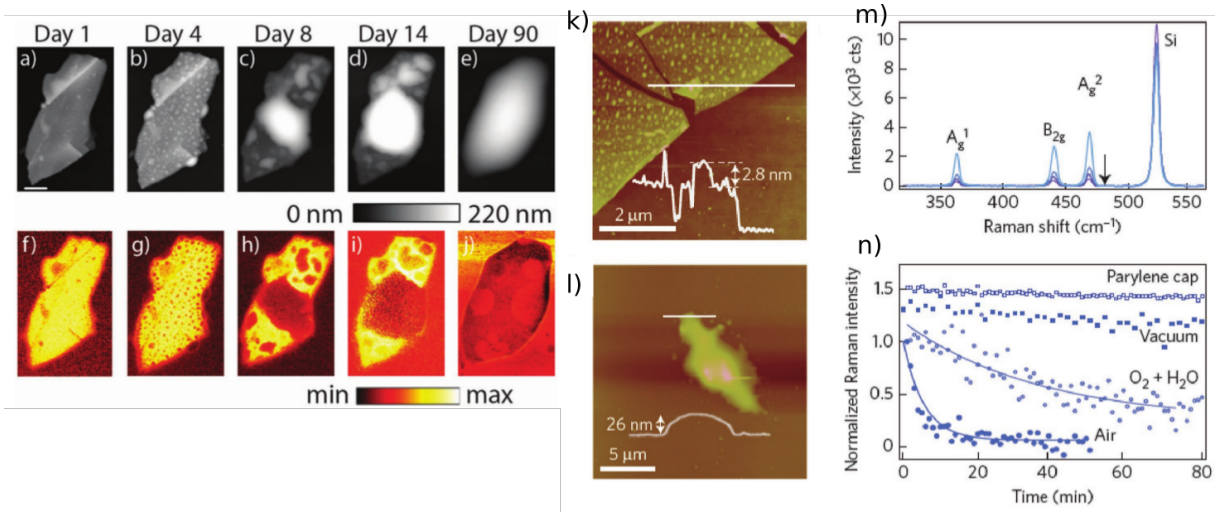

Figure 8: Time evolution of: (a)-(e) topography and (f)-(j) near-field third harmonic optical amplitude taken at a laser wavelength of 10μm of freshly exfoliated unencapsulated BP with thickness of 27 nm. (k) AFM images taken from another study of freshly exfoliated BP and (l) after a few days later in ambient conditions. (m) Raman spectra of a 5 nm thick sample measured in air. (n) Time dependence of the integrated intensity of the Ag^2 Raman mode in different conditions. The experiments were made with constant laser illumination. Figure adapted from Refs. [48, 49].

1.5 Topological Phase Transition in Phosphorene

It has been both theoretically predicted and experimentally demonstrated that BP can undergo a transition from a semiconducting phase to a semi-metallic phase by a number of different mechanisms, which include: applying a perpendicular electric field through external gates [51, 52]; the application of hydrostatic pressure [53, 54, 55]; surface doping of the BP crystal and also the incidence of rapidly oscillating laser fields [56, 57, 59]. The material responds to these external inputs by changing progressively its band structure up to and beyond a critical point where its *topology* near the Fermi level is altered. The band gap is gradually reduced to the point where the bottom of the conduction band touches the top of the valence band. At this point, a Dirac cone emerges in the Brillouin zone. With further increase of the external parameter, a band inversion takes place. Such transition can be seen in maps of constant energy where the topology of the Fermi surface is shown to gradually change.

This transition was predicted to happen under strain using the $\mathbf{k} \cdot \mathbf{p}$ approximation and DFT calculations. It was suggested that this prediction could be experimentally detected via the unusual Landau levels it was expected to produce [54]. This prediction was confirmed by measuring the transport properties of few-layer BP under high-pressures at various temperatures. It was observed that, for pressures higher than a critical value of $P = 1.2$ GPa, the BP sample showed metallic longitudinal resistivity (ρ_{xx}) in the entire temperature range, from 2 to 300 K [53]. Calculations of the transversal resistivity (ρ_{xy}) as a function of the perpendicularly applied magnectic field revealed a nonlinear behavior for $P > P_c = 1.2$ GPa, which is a char-

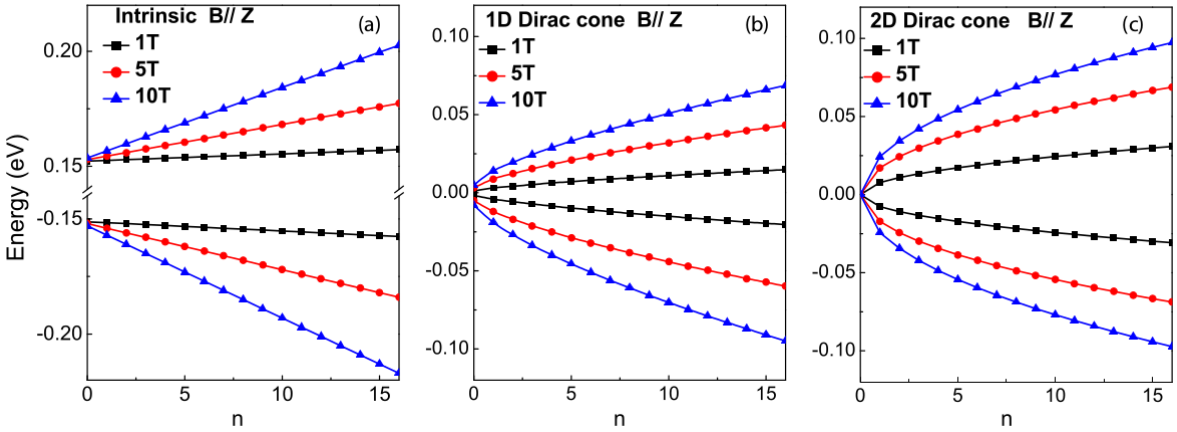

Figure 9: The energy spectrum of Landau levels (index n) of (a) intrinsic BP with magnetic field, (b) under critical pressure, in which 1D Dirac cone is formed and (c) beyond the critical pressure, in which 2D Dirac cones are formed. Figure extracted from Ref. [54].

acteristic of multiband conduction. Furthermore, for values of pressure at the vicinity of P_c, the magnetoresistance was enhanced by a factor of ~ 40 and reached the value of $\sim 80000\%$ in a magnetic field of 9 T. Such phenomenon is also common in various semimetals and is attributed to electron-hole compensation.

The emergence of unusual Landau levels have been proposed as yet another way to detect such phase transition [54]. Instead of being proportional to the energy level index n, as in regular semiconductors, the energy levels depends on the square root of n, much like in graphene, see Fig. (9). Recently, a theoretical studied which included the effects of strain in a simple tight-binding Hamiltonian reveleaed that strain along the z and x directions are able to caus ethe phase transition, whereas strains along the y direction could reduce but never fully close the band gap [55].

The application of a perpendicular field can also produce the same phase transition in multilayer BP, as found in a theoretical study by Yuan *et al* using a simple tight-binding model including the electric field effect into the Hamiltonian by adding an appropriate on-site symmetric potential $\propto \Delta$ to each layer [51]. They found the energy gap to be gradually reduced with increasing values of Δ to a point where the gap closed. Beyond that point, a Dirac cone was observed in the vicinity of the Fermi level in the $\Gamma \rightarrow X$ direction of the Brillouin zone. Furthermore, maps of constant energy showed the gradual transition of the band structure from an elliptical to a ring-like topology [51]. Theoretical and experimental works have shown that it is also possible to induce this phase transition via surface doping with potassium and cesium atoms [56, 57, 58]. The band structure of BP in the band-inverted regime was obtained by means of high-resolution angle resolved photoemission spectroscopy (ARPES), as can be seen in Figs. 10 (d)-(f). These Dirac cones have been shown to be topologically protected by space-time inversion symmetry even in the presence of spin-orbit coupling [57].

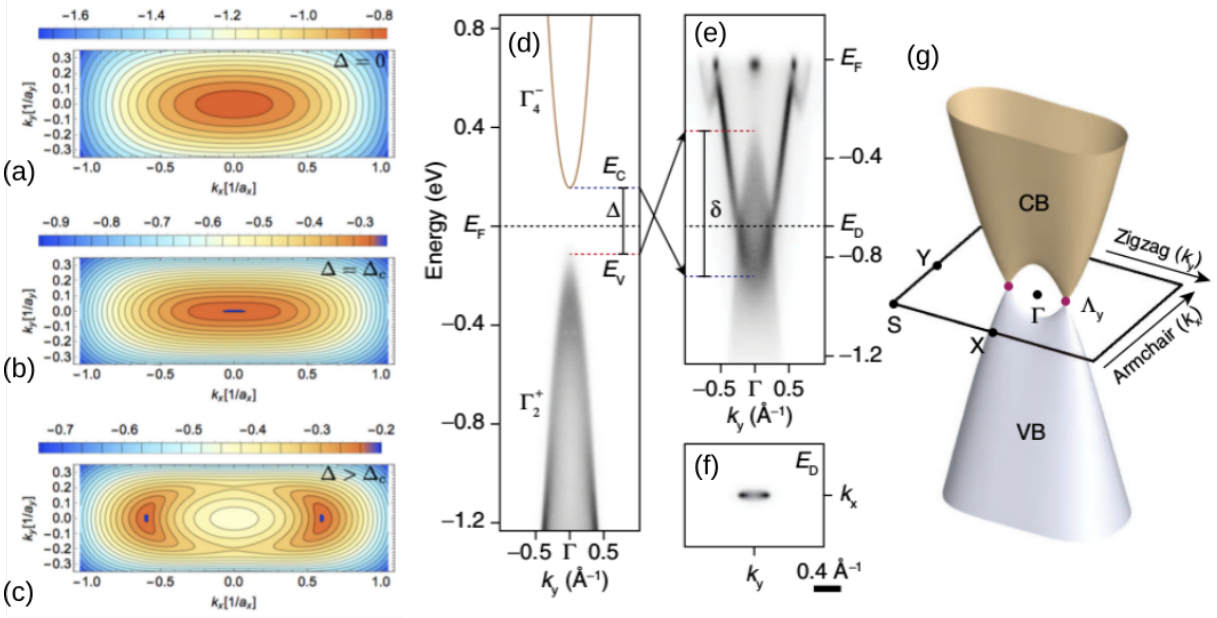

Figure 10: (a)-(c) Constant energy contours of biased bilayer BP for three values of applied voltage calculated within a tight-binding model. Experimental band structure of BP near the Γ point along k_y (d) before and (e) after surface doping. The dark yellow line in (d) shows the an unoccupied CB, obtained from tight-binding calculations. Blue and red dotted lines denote the maximum of energy of Γ_2^+ and the minimum of energy Γ_4^- states, respectively, which are inverted between (a) and (b), as indicated by arrows. (f) Constant-energy map at E_D taken from BP at the same doping level as in (e). (g) Illustration of the band structure of biased BP, where the Brillouin zone, Dirac points and high-symmetry points are highlighted. Figure adapted from Refs. [51, 57].

1.6 Structure of the Monograph

In the present chapter, a general overview of BP, particularly in its 2D form (phosphorene), has been made, including a number of properties that set it apart from other materials. In the second chapter, the band structure of mono and bilayer phosphorene will be obtained by means of a tight-binding model, as well as an extension to the model to calculate the band structure to any number of layers (multilayer phosphorene). In the third chapter, a study of the topological transition in multilayer phosphorene will be made, using the bilayer as a prototype, including the effects on the carrier concentration of infinite and confined systems (nanoribbons). Finally, the last chapter will present the concluding remarks and perspectives for future explorations.

2 MULTILAYER PHOSPHORENE: A TIGHT-BINDING APPROACH

This chapter presents a method of obtaining the band structure of multilayer BP from a tight-binding method, based on a model proposed by Rudenko *et al* [60]. In the first section, it will be shown that this can be achieved by writing the Hamiltonian in second quantization formalism and by exploiting the Fourier transformations of the field operators associated with each sublattice in order to diagonalize the resulting Hamiltonian. An analogous calculation is performed for a system with two layers (bilayer BP), with the additional terms corresponding to the extra sublattices and the coupling between the layers. Finally, the method is extended to a system containing an arbitrary number of layers (multilayer BP). This development follows closely that of Ref. [61].

2.1 Single Layer

Consider an infinite sheet of BP such as the one shown in Figure 1. At least four basis atoms are required in order to construct the crystalline structure of phosphorene. Each of these four atoms belong to a sublattice that is symmetric across unit cells and they are thus labeled A, B, C and D, and the amplitudes to find a particle in each of the sublattices are represented by ϕ_A, ϕ_B, ϕ_C and ϕ_D, respectively. Let the TB Hamiltonian in second quantization be:

$$\mathcal{H} = \sum_i \epsilon_i g_i^\dagger g_i + \sum_{i,j} t_{ij} g_i^\dagger g_j, \tag{2.1}$$

where ϵ_i are the on-site energies at atomic sites i, t_{ij} are the hopping parameters between sites i and j and $g_i^\dagger$, g_i are the respective creation and anihilation operators associated with an arbitrary sublattice. The sum runs over all atomic sites. The dispersion relation can be obtained by substituting the Fourier transform of the field operators into (2.1) and, after some algebra and exploitation of symmetry properties, solving the eigenvalue problem originating from the time-independent Schrodinger equation. The Fourier transformation of the field operators is given by :

$$g_i = \frac{1}{\sqrt{N}} \sum_k e^{i\mathbf{k}\cdot\mathbf{r}_i} g_k, \qquad g_i^\dagger = \frac{1}{\sqrt{N}} \sum_k e^{-i\mathbf{k}\cdot\mathbf{r}_i} g_k^\dagger, \tag{2.2}$$

where N is the number of unit cells in the system and $g_k^\dagger$, g_k create and destroy particles with wave-vector k in an arbitrary sublattice in reciprocal space. Substituting (2.2) into (2.1), one obtains:

$$\mathcal{H} = \frac{1}{N} \sum_i \sum_{k,k'} \epsilon_i e^{i\mathbf{k}\cdot\mathbf{r}_i} e^{-i\mathbf{k}'\cdot\mathbf{r}_i} g_{k'}^\dagger g_k + \frac{1}{N} \sum_{i,j} \sum_{k,k'} t_{ij} e^{i\mathbf{k}\cdot\mathbf{r}_i} e^{-i\mathbf{k}'\cdot\mathbf{r}_j} g_{k'}^\dagger g_k. \tag{2.3}$$

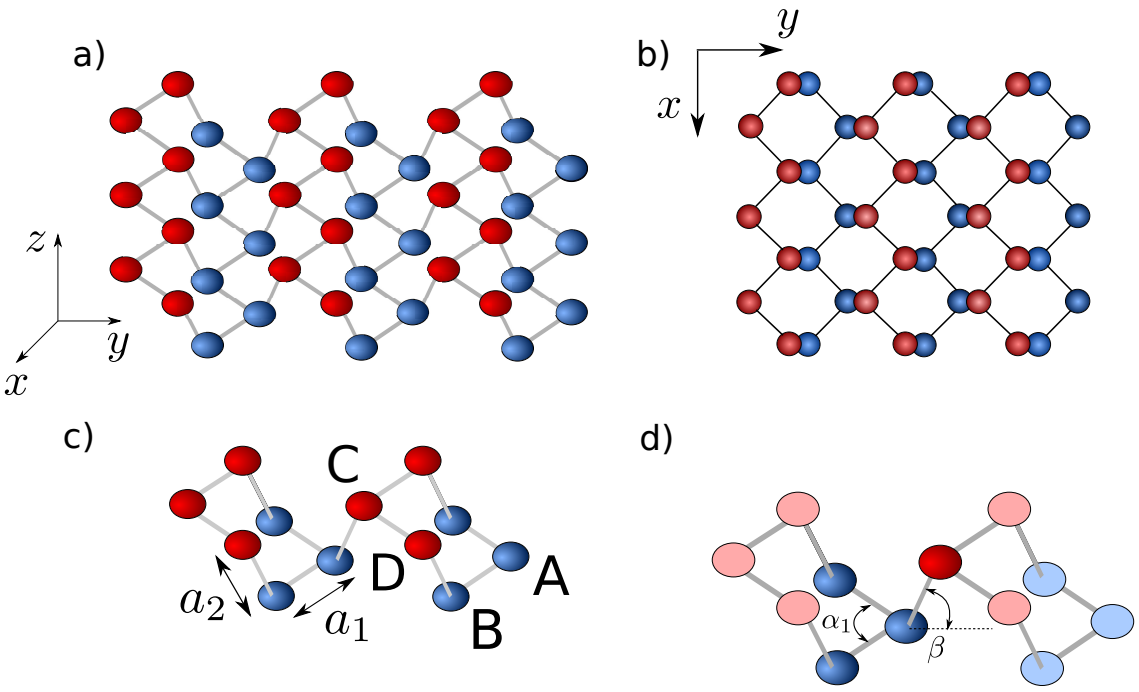

Figure 11: Geometry of a phosphorene monolayer. (a) Puckered crystalline structure seen from an angle and (b) seen from the top, highlighting the axis orientation and the unit cell. The bond angles and bond lengths are shown in (c) and (d), respectively.

Now, let $\delta_n^m = \mathbf{r}_j - \mathbf{r}_i$ be the xy plane projection of the n-th vector connecting the atomic site i and j, where i is called the *origin* and j is the *target* site at the sublattice m. From now on, the δ_n^m's will be called *hopping vectors*. So, for instance, if a particle is at the sublattice A (origin site), there are six target sites at the sublattice B it can hop to within this model: two first neighbours via t_1 with hopping vectors δ_1^B and δ_2^B; two third nearest neighbours via t_4 with hopping vectors δ_3^B and δ_4^B; two third nearest neighbours via t_8 with hopping vectors δ_5^B and δ_6^B. In order not to interrupt the flow of the text, the calculation of the δ_n^m will be left to the Appendix. Therefore, substituting $\mathbf{r}_j = \delta_n^m + \mathbf{r}_i$ in equation (2.3), one obtains:

$$\begin{aligned}
\mathcal{H} &= \frac{1}{N}\sum_i\sum_{k,k'} \epsilon_i e^{i(\mathbf{k}-\mathbf{k}')\cdot\mathbf{r}_i} g_{k'}^\dagger g_k + \frac{1}{N}\sum_{i,j}\sum_{k,k'} t_{ij} e^{\mathbf{k}\cdot\mathbf{r}_i} e^{-i\mathbf{k}'\cdot(\mathbf{r}_i+\delta_n^m)} g_{k'}^\dagger g_k \\
&= \frac{1}{N}\sum_i\sum_{k,k'} \epsilon_i e^{i(\mathbf{k}-\mathbf{k}')\cdot\mathbf{r}_i} g_{k'}^\dagger g_k + \frac{1}{N}\sum_{i,j}\sum_{k,k'} t_{ij} e^{i(\mathbf{k}-\mathbf{k}')\cdot\mathbf{r}_i} e^{-i\mathbf{k}'\cdot\delta_n^m} g_{k'}^\dagger g_k \\
&= \sum_i \mathcal{H}_i + \sum_{i,j} \mathcal{H}_{i\to j(i\neq j)},
\end{aligned}$$

where $i, j = A, B, C, D$. Thus, the Hamiltonian can be separated into one term associated with the on-site energies,

$$\mathcal{H}_{\text{onsite}} = \sum_{\text{all sites}} (\mathcal{H}_A + \mathcal{H}_B + \mathcal{H}_C + \mathcal{H}_D), \tag{2.4}$$

and a term collecting all the hopping contributions between each sublattice,

$$\mathcal{H}_{\text{hopping}} = \sum_{\text{all sites}} (\mathcal{H}_{A\to A} + \mathcal{H}_{A\to B} + \mathcal{H}_{A\to C} + \mathcal{H}_{A\to D} + \mathcal{H}_{B\to A} + \mathcal{H}_{B\to B} + ...). \tag{2.5}$$

For an origin site at the sublattice A, the hopping terms $\mathcal{H}_{i\to j}$ are:

$$\begin{aligned}\mathcal{H}_{A\to A} = \frac{1}{N}\sum_i \sum_{k,k'} e^{i(\mathbf{k}-\mathbf{k}')}[t_3(e^{-i\mathbf{k}'\cdot\delta_1^A} + e^{-i\mathbf{k}'\cdot\delta_2^A}) + t_7(e^{-i\mathbf{k}'\cdot\delta_3^A} + e^{-i\mathbf{k}'\cdot\delta_4^A}) \\ + t_{10}(e^{-i\mathbf{k}'\cdot\delta_5^A} + e^{-i\mathbf{k}'\cdot\delta_6^A} + e^{-i\mathbf{k}'\cdot\delta_7^A} + e^{-i\mathbf{k}'\cdot\delta_8^A})]a_k^\dagger a_k \end{aligned} \tag{2.6}$$

$$\begin{aligned}\mathcal{H}_{A\to B} = \frac{1}{N}\sum_i \sum_{k,k'} e^{i(\mathbf{k}-\mathbf{k}')}[t_1(e^{-i\mathbf{k}'\cdot\delta_1^B} + e^{-i\mathbf{k}'\cdot\delta_2^B}) + t_4(e^{-i\mathbf{k}'\cdot\delta_3^B} + e^{-i\mathbf{k}'\cdot\delta_4^B}) \\ + t_8(e^{-i\mathbf{k}'\cdot\delta_1^5} + e^{-i\mathbf{k}'\cdot\delta_6^B})]b_k^\dagger a_k \end{aligned} \tag{2.7}$$

$$\mathcal{H}_{A\to C} = \frac{1}{N}\sum_i \sum_{k,k'} e^{i\mathbf{k}-\mathbf{k}')}[t_2 e^{-i\mathbf{k}'\cdot\delta_1^C} + t_6 e^{-i\mathbf{k}'\cdot\delta_2^C} + t_9(e^{-i\mathbf{k}'\cdot\delta_3^C} + e^{-i\mathbf{k}'\cdot\delta_4^C})]c_k^\dagger a_k \tag{2.8}$$

$$\mathcal{H}_{A\to D} = \frac{1}{N}\sum_i \sum_{k,k'} e^{i(\mathbf{k}-\mathbf{k}')}[t_5(e^{-i\mathbf{k}'\cdot\delta_1^D} + e^{-i\mathbf{k}'\cdot\delta_2^D} + e^{-i\mathbf{k}'\cdot\delta_3^D} + e^{-i\mathbf{k}'\cdot\delta_4^D})]d_k^\dagger a_k \tag{2.9}$$

The equations above can be simplified by using the following identity:

$$\delta_{kk'} = \frac{1}{N}\sum_i e^{i(\mathbf{k}-\mathbf{k}')\cdot\mathbf{r}_i}, \tag{2.10}$$

which is none other than the discrete Fourier transform of the Dirac delta function. Substituting eq. (2.10) in the hopping terms, the hopping sub-Hamiltonian from A to A becomes:

$$\begin{aligned}\mathcal{H}_{A\to A} &= \sum_{k,k'} \delta_{kk'}[t_3(e^{-\mathbf{k}'\cdot\delta_1^A} + e^{-i\mathbf{k}'\cdot\delta_2^A}) + t_7(e^{-i\mathbf{k}'\cdot\delta_3^A} + e^{-i\mathbf{k}'\cdot\delta_4^A}) \\ &\quad + t_{10}(e^{-i\mathbf{k}'\cdot\delta_5^A} + e^{-i\mathbf{k}'\cdot\delta_6^A} + e^{-i\mathbf{k}'\cdot\delta_7^A} + e^{-i\mathbf{k}'\cdot\delta_8^A})]a_k^\dagger a_k \\ &= \sum_k [t_3(e^{-i\mathbf{k}\cdot\delta_1^A} + e^{-i\mathbf{k}\cdot\delta_2^A}) + t_7(e^{-i\mathbf{k}\cdot\delta_3^A} + e^{-i\mathbf{k}\cdot\delta_4^A}) \\ &\quad + t_{10}(e^{-i\mathbf{k}\cdot\delta_5^A} + e^{-i\mathbf{k}\cdot\delta_6^A} + e^{-i\mathbf{k}\cdot\delta_7^A} + e^{-i\mathbf{k}\cdot\delta_8^A})]a_k^\dagger a_k \\ &= \sum_k t_{AA}(k) a_k^\dagger a_k, \end{aligned} \tag{2.11}$$

where $t_{AA}(k)$ is the *structure factor* given by:

$$\begin{aligned}t_{AA}(k) &= 2t_3\cos[2a_1\sin(\alpha_1/2)k_x] \\ &\quad + 2t_7\cos\{2a_1\cos(\alpha_1/2) + 2a_2\cos\beta]k_y\} \\ &\quad + 4t_{10}\cos[2a_1\cos(\alpha_1/2)k_x]\cos\{2a_1\cos(\alpha_1/2) + 2a_2\cos\beta]k_y\}. \end{aligned} \tag{2.12}$$

The remaining terms as well as their respective structure factors are calculated explicitly in the

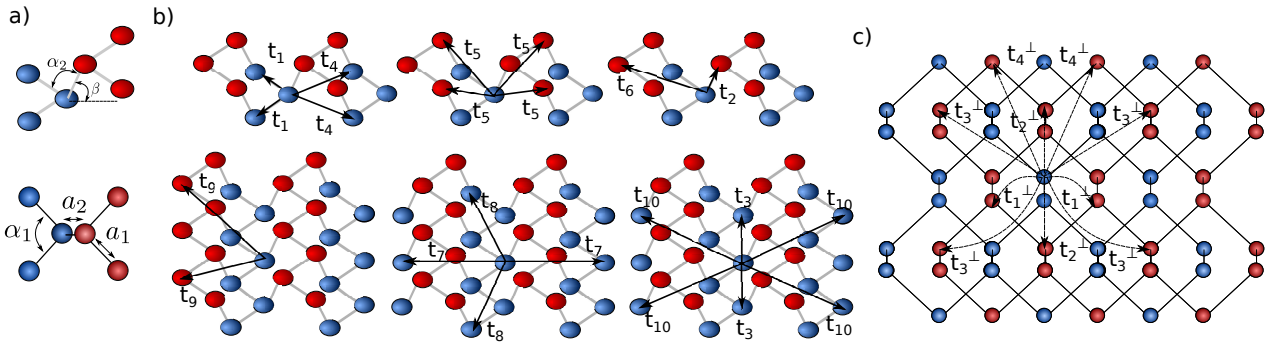

Figure 12: Lattice structure of multilayer BP systems and parameters for the tight-binding model. (a) Definitions of the bond lengths and bond angles. Sketches of the (b) 10-intralayer and (c) four-intralayer hopping parameters. Figure adapted from Ref. [61]

Appendix. Their structure factors are given by:

$$\begin{aligned} t_{AB}(k) &= 2t_1 \cos[a_1 \sin(\alpha_1/2)k_x] e^{ia_1 \cos(\alpha_1/2)k_y} \\ &\quad + 2t_4 \cos[a_1 \sin(\alpha_1/2)k_x] e^{-i[2a_2 \cos\beta + a_1 \cos(\alpha_1/2)]k_y} \\ &\quad + 2t_8 \cos[3a_1 \sin(\alpha_1/2)k_x] e^{ia_1 \cos(\alpha_1/2)k_y}, \end{aligned} \tag{2.13}$$

$$\begin{aligned} t_{AC}(k) &= t_2 e^{-ia_2 \cos(\beta)k_y} + t_6 e^{i[a_2 \cos\beta + 2a_1 \cos(\alpha_1/2)]k_y} \\ &\quad + 2t_9 \cos[2a_1 \sin(\alpha_1/2)k_x] e^{i[a_2 \cos\beta + 2a_1 \cos(\alpha_1/2)]k_y} \end{aligned} \tag{2.14}$$

$$t_{AD}(k) = 4t_5 \cos[a_1 \sin(\alpha_1/2)k_x] \cos\{[a_1 \cos(\alpha_1/2) + a_2 \cos\beta]k_y\}. \tag{2.15}$$

The onsite sub-Hamiltonian is:

$$\mathcal{H}_{\text{onsite}} = \sum_k (\epsilon_A a_k^\dagger a_k + \epsilon_B b_k^\dagger b_k + \epsilon_C c_k^\dagger c_k + \epsilon_D d_k^\dagger d_k) \tag{2.16}$$

Therefore, the complete Hamiltonian takes the following form:

$$\begin{aligned} \mathcal{H} = &\sum_k [(\epsilon_A + t_{AA}(k)) a_k^\dagger + t_{AB}(k) b_k^\dagger + t_{AC}(k) c_k^\dagger + + t_{AD}(k) d_k^\dagger] a_k \\ &+ \sum_k [t_{BA}(k) a_k^\dagger + (\epsilon_B + t_{BB}(k)) b_k^\dagger + t_{BC}(k) c_k^\dagger + + t_{BD}(k) d_k^\dagger] b_k \\ &+ \sum_k [t_{CA}(k) a_k^\dagger + t_{CB}(k)) b_k^\dagger + (\epsilon_C + t_{CC}(k)) c_k^\dagger + t_{CD}(k) d_k^\dagger] c_k \\ &+ \sum_k [t_{DA}(k) a_k^\dagger + t_{DB}(k)) b_k^\dagger + t_{DC}(k) c_k^\dagger + (\epsilon_D + t_{DD}(k)) d_k^\dagger] d_k. \end{aligned} \tag{2.17}$$

One needs the most general state vector of the system that the Hamiltonian can act upon in order to form the complete eigenvalue problem. In second quantization, it is obtained by acting the sublattice-specific creation operators onto a vacuum state represented by $|0\rangle$ as follows:

$$|\Psi\rangle = \sum_k (\phi_A a_k^\dagger + \phi_B b_k^\dagger + \phi_C c_k^\dagger + \phi_D d_k^\dagger) |0\rangle . \tag{2.18}$$

Thus, from the time-independent Schrodinger equation for a particular k state, the following eigenvalue problem is obtained:

$$\mathcal{H}_k \left|\Psi_k\right\rangle = E_k \left|\Psi_k\right\rangle \tag{2.19}$$

Using equations (2.17) and (2.18), the following equations are obtained:

$$\begin{aligned}
(\epsilon_A + t_{AA}(k))\phi_A + t_{BA}(k)\phi_B + t_{DA}(k)\phi_D + t_{CA}(k)\phi_C &= E_k\phi_A \\
t_{AB}(k)\phi_A + (\epsilon_B + t_{BB}(k))\phi_B + t_{DB}(k)\phi_D + t_{CB}(k)\phi_C &= E_k\phi_B \\
t_{AD}(k)\phi_A + t_{BD}(k)\phi_B + (\epsilon_D + t_{DD}(k))\phi_D + t_{CD}(k)\phi_C &= E_k\phi_D \\
t_{AC}(k)\phi_A + t_{BC}(k)\phi_B + t_{DC}(k)\phi_D + (\epsilon_C + t_{CC}(k))\phi_C &= E_k\phi_C
\end{aligned} \tag{2.20}$$

which can be expressed in matrix form:

$$\begin{pmatrix}
\epsilon_A + t_{AA}(k) & t_{AB}(k) & t_{AD}(k) & t_{AC}(k) \\
t_{BA}(k) & \epsilon_B + t_{BB}(k) & t_{BD}(k) & t_{BC}(k) \\
t_{DA}(k) & t_{DB}(k) & \epsilon_D + t_{DD}(k) & t_{DC}(k) \\
t_{CA}(k) & t_{CB}(k) & t_{CD}(k) & \epsilon_C + t_{CC}
\end{pmatrix}
\begin{pmatrix} \phi_A \\ \phi_B \\ \phi_D \\ \phi_C \end{pmatrix}
= E_k
\begin{pmatrix} \phi_A \\ \phi_B \\ \phi_D \\ \phi_C \end{pmatrix}. \tag{2.21}$$

Setting $\epsilon_i = 0$, for simplicity, the Hamiltonian matrix can be written as:

$$\mathcal{H}_k = \begin{pmatrix}
t_{AA}(k) & t_{BA}(k) & t_{DA}(k) & t_{CA}(k) \\
t^*_{AB}(k) & t^*_{AA}(k) & t^*_{DB}(k) & t_{CB}(k) \\
t_{AD}(k) & t_{BD}(k) & t_{AA}(k) & t_{CD}(k) \\
t^*_{AC}(k) & t_{BC}(k) & t^*_{DC}(k) & t_{AA}(k)
\end{pmatrix}. \tag{2.22}$$

Further simplification ensues from noting that, since this Hamiltonian must be hermitian, $t_{ij}(k) = t^*_{ji}(k)$ and also from exploiting several symmetry properties which are discussed in detail in the Appendix B. By employing this scheme, the Hamiltonian can be written as:

$$\mathcal{H}_k = \begin{pmatrix}
t_{AA}(k) & t_{AB}(k) & t_{AD}(k) & t_{AC}(k) \\
t^*_{AB}(k) & t^*_{AA}(k) & t^*_{AC}(k) & t_{AD}(k) \\
t_{AD}(k) & t_{AC}(k) & t_{AA}(k) & t_{AB}(k) \\
t^*_{AC}(k) & t_{AD}(k) & t^*_{AB}(k) & t_{AA}(k)
\end{pmatrix}. \tag{2.23}$$

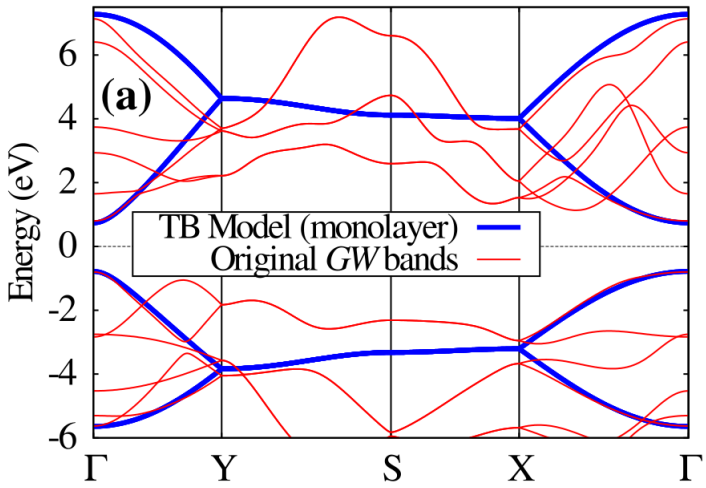

Figure 13: Energy bands obtained from the TB Hamiltonian (blue lines) in comparison with the ones obtained by DFT-GW that was used to get the hopping parameters from. Figure adapted from Ref. [60].

A suitable unitary transformation can put the Hamiltonian matrix and the eigenstates in the basis of the combination of atomic orbitals, which is given by the following expression:

$$U = \frac{1}{\sqrt{2}} \begin{pmatrix} 1 & 0 & 1 & 0 \\ 0 & 1 & 0 & 1 \\ 1 & 0 & -1 & 0 \\ 0 & 1 & 0 & -1 \end{pmatrix} \tag{2.24}$$

The new Hamiltonian and eigenvector are thus given by $\mathcal{H}'_k = U^\dagger \mathcal{H}_k U$ and $|\psi'_k\rangle = U\,|\psi_k\rangle$, respectively, where:

$$\mathcal{H}'_k = \begin{pmatrix} t_{AA}(k) + t_{AD}(k) & t_{AB}(k) + t_{AC}(k) & 0 & 0 \\ t^*_{AC}(k) + t_{AB} & t_{AA}(k) + t_{AD}(k) & 0 & 0 \\ 0 & 0 & t_{AA}(k) - t_{AD}(k) & t_{AB}(k) - t_{AC}(k) \\ 0 & 0 & t^*_{AB}(k) - t^*_{AD}(k) & t_{AA}(k) - t_{AD}(k) \end{pmatrix}, \tag{2.25}$$

and

$$|\psi_k\rangle = \begin{pmatrix} \phi_A + \phi_D \\ \phi_B + \phi_C \\ \phi_A - \phi_D \\ \phi_B - \phi_C \end{pmatrix} \tag{2.26}$$

The form of the eigenvectors $|\psi_k\rangle$ suggests the symmetry between the A, D and the B, C

Table 1: Hopping parameters of the GW-based TB model.

Parameter	Value (eV)	Parameter	Value (eV)
t_1	-1.486	t_2	3.729
t_3	-0.252	t_4	-0.071
t_5	-0.019	t_6	0.186
t_7	-0.063	t_8	0.101
t_9	-0.042	t_10	0.073
$t_1^\perp$	0.524	$t_2^\perp$	0.180
$t_3^\perp$	-0.123	$t_4^\perp$	-0.168

sublattices. The above Hamiltonian and eigenstates can be more simply written as:

$$\mathcal{H}'_k = \begin{pmatrix} H_k^+ & 0 \\ 0 & H_k^- \end{pmatrix} \text{ and } \quad \psi'_k = \begin{pmatrix} \Psi_k^+ \\ \Psi_k^- \end{pmatrix}, \tag{2.27}$$

where

$$H_k^\pm = H_0 \pm H_2 \text{ and } \quad \Psi_k^\pm = \begin{pmatrix} \phi_A \pm \phi_D \\ \phi_B \pm \phi_C \end{pmatrix}, \tag{2.28}$$

with

$$H_0 = \begin{pmatrix} t_{AA}(k) & t_{AB}(k) \\ t_{AB}^*(k) & t_{AA}(k) \end{pmatrix} \text{ and } \quad H_2 = \begin{pmatrix} t_{AD}(k) & t_{AC}(k) \\ t_{AC}^*(k) & t_{AD}(k) \end{pmatrix}. \tag{2.29}$$

The diagonalization of this Hamiltonian leads to the following bands:

$$E_s^\pm(k) = t_{AA}(k) \pm t_{AD}(k) + s|t_{AB}(k) \pm t_{AC}(k)|, \tag{2.30}$$

where $s = \pm$ denotes the valence (+) and conduction (-) bands, respectively. A detailed analysis of this equation reveals that the bands associated with $E_s^+(k)$ have lower energies than the bands associated with $E_s^-(k)$. The energy gap for single-layer BP is thus calculated from the eigenvalues of H_k^+ at the Γ point, that is:

$$E_g^{\text{mono}} = 2|t_{AB}(0) + t_{AC}(0)| \approx 1.838 \text{ eV} \tag{2.31}$$

2.2 Bilayer

The calculation of the energy bands for the bilayer case is analogous to the previous section, with the addition of the five interlayer hopping parameters. The new hoppings and their hopping vectors are depicted in Figure. Since this system has eight atoms in its basis, the

Hamiltonian matrix is 8×8 [62]:

$$\mathcal{H}_{\text{bilayer}} = \begin{pmatrix} H_0 & H_2 & 0 & 0 \\ H_2 & H_0 & H_3 & 0 \\ 0 & H_3 & H_0 & H_2 \\ 0 & 0 & H_2 & H_0 \end{pmatrix}, \tag{2.32}$$

where:

$$H_3 = \begin{pmatrix} t_{AD'}(k) & t_{AC'}(k) \\ t^*_{AC'}(k) & t^*_{AD'}(k) \end{pmatrix}. \tag{2.33}$$

This matrix can be more simply written as:

$$\mathcal{H}_{\text{bilayer}} = \begin{pmatrix} H & H_c^\dagger \\ H_c & H \end{pmatrix}, \tag{2.34}$$

where:

$$H = \begin{pmatrix} H_0 & H_2 \\ H_2 & H_0 \end{pmatrix} \text{ and } \quad H_c = \begin{pmatrix} 0 & H_3 \\ 0 & 0 \end{pmatrix}. \tag{2.35}$$

It's important to note that the bilayer Hamiltonian is a tridiagonal matrix where the main diagonal consists of monolayer-like terms and the adjacent diagonals consist of terms associated with the interaction between layers. Similarly to the single-layer case, a unitary transformation (Appendix) is applied in order to simplify the form of the Hamiltonian matrix. The resulting Hamiltonian is:

$$\mathcal{H}_k^{\pm} = \begin{pmatrix} H_0 \pm H_2 + H_3/2 & 0 \\ 0 & H_0 \pm H_2 - H_3/2 \end{pmatrix}, \tag{2.36}$$

where the Hamiltonians $\mathcal{H}_k^+$ and $\mathcal{H}_k^-$ describe low and high energy bands, respectively. Except for the interaction sub-Hamiltonian H_3, the bilayer Hamiltonian is very similar to the monolayer one. The eigenstates of Hamiltonian $\mathcal{H}_k^{\pm}$ are:

$$\Psi_k^{\pm} = \frac{e^{i\theta_\pm}}{2} \begin{pmatrix} (\phi_A^1 \pm \phi_D^1) + (\phi_A^2 \pm \phi_D^2) \\ (\phi_B^1 \pm \phi_C^1) + (\phi_B^2 \pm \phi_C^2) \\ (\phi_A^1 \pm \phi_D^1) + (\phi_A^2 \pm \phi_D^2) \\ (\phi_B^1 \pm \phi_C^1) + (\phi_B^2 \pm \phi_C^2) \end{pmatrix}, \tag{2.37}$$

where the subscript represents the sublattice index and the superscript represents the layer index (1 is the first layer and 2 is the second layer) and $\theta_+ = 0$ and $\theta_- = \pi/2$. The diagonalization of

this Hamiltonian yields the following energy bands close to the Fermi level:

$$E_c = \frac{1}{2}[(\epsilon_1^+ + \epsilon_2^+ + \epsilon_1^- + \epsilon_2^-) \pm (\epsilon_1^+ + \epsilon_2^+ - \epsilon_1^- - \epsilon_2^-)],$$
$$E_v = \frac{1}{2}[(\epsilon_1^+ - \epsilon_2^+ + \epsilon_1^- - \epsilon_2^-) \pm (\epsilon_1^+ - \epsilon_2^+ - \epsilon_1^- + \epsilon_2^-)], \tag{2.38}$$

where E_c and E_v are the conduction and valence bands, respectively, and:

$$\epsilon_1^\pm = t_{AA}(k) + t_{AD}(k) \pm t_{AD'}(k)/2,$$
$$\epsilon_2^\pm = |t_{AB}(k) + t_{AC}(k) \pm t_{AC'}(k)/2| \tag{2.39}$$

The energy gap can be calculated by evaluating $E_c - E_v$ at $k = 0$, from which we obtain that $E_g^{\text{bi}} \approx 1.126$ eV.

2.3 An extension to Multilayer

In this section, the tight-binding model developed in the previous sections will be extended to a BP system with an arbitrary number of layers. A natural generalization of the Hamiltonian (2.32) would include a main diagonal composed of monolayer-like terms and adjacent diagonals composed of interlayer interaction terms:

$$\mathcal{H}_N = \begin{pmatrix} H & H_c & & & & \\ H_c^\dagger & H & H_c & & & \\ & H_c^\dagger & H & H_c & & \\ & & & \ddots & H_c^\dagger & \\ & & & H_c^\dagger & H & \end{pmatrix}_{N\times N}. \tag{2.40}$$

Since only immediately neighbouring layers interact, all the other matrix elements are zero. The eigenvectors of this Hamiltonian is the N-dimensional pseudospinor:

$$\Psi_N = \begin{pmatrix} \Phi_1 \\ \Phi_2 \\ \vdots \\ \Phi_N \end{pmatrix}, \quad \text{where} \quad \Phi_i = \begin{pmatrix} \phi_{A,i} \\ \phi_{B,i} \\ \phi_{D,i} \\ \phi_{C,i}. \end{pmatrix}. \tag{2.41}$$

The eigenvalue problem resulting from the time-independent Schrodinger equation yields a number of equations with the form:

$$H_c^\dagger \Phi_{i-1} + (H - E)\Phi_i + H_c \Phi_{i+1} = 0, \tag{2.42}$$

where $i = 1, 2, 3, ..., N$ represents the layer index and the suitable boundary condition is $\Phi_0 = \Phi_N + 1 = 0$. Writing this equation more explicitly, one obtains:

$$\begin{pmatrix} 0 & H_3 \\ 0 & 0 \end{pmatrix} \begin{pmatrix} \phi_{A,i-1} \\ \phi_{B,i-1} \\ \phi_{D,i-1} \\ \phi_{C,i-1} \end{pmatrix} + \begin{pmatrix} H_0 - E & H_2 \\ H_2 & H_0 - E \end{pmatrix} \begin{pmatrix} \phi_{A,i} \\ \phi_{B,i} \\ \phi_{D,i} \\ \phi_{C,i} \end{pmatrix} + \begin{pmatrix} 0 & 0 \\ H_3 & 0 \end{pmatrix} \begin{pmatrix} \phi_{A,i+1} \\ \phi_{B,i+1} \\ \phi_{D,i+1} \\ \phi_{C,i+1} \end{pmatrix} = 0. \quad (2.43)$$

Now, to proceed further, we rewrite the eigenstate spinor as:

$$\psi_{AB,j} = \begin{pmatrix} \phi_{A,j} \\ \phi_{B,j} \end{pmatrix} \text{ and } \quad \psi_{DC,j} = \begin{pmatrix} \phi_{D,j} \\ \phi_{C,j} \end{pmatrix}. \quad (2.44)$$

Therefore:

$$\begin{pmatrix} 0 & H_3 \\ 0 & 0 \end{pmatrix} \begin{pmatrix} \psi_{AB,i-1} \\ \psi_{DC,i-1} \end{pmatrix} + \begin{pmatrix} H_0 - E & H_2 \\ H_2 & H_0 - E \end{pmatrix} \begin{pmatrix} \psi_{AB,i} \\ \psi_{DC,i} \end{pmatrix} + \begin{pmatrix} 0 & 0 \\ H_3 & 0 \end{pmatrix} \begin{pmatrix} \psi_{AB,i+1} \\ \psi_{DC,i+1} \end{pmatrix} = 0$$
$$\begin{pmatrix} H_3\psi_{DC,i-1} \\ 0 \end{pmatrix} + \begin{pmatrix} (H_0 - E)\psi_{AB,i} + H_2\psi_{DC,i} \\ H_2\psi_{AB,i} + (H_0 - E)\psi_{DC,i} \end{pmatrix} + \begin{pmatrix} 0 \\ H_3\psi_{AB,i+1} \end{pmatrix} = 0 \quad (2.45)$$

which leads to the following pair of equations for each i:

$$\begin{aligned} (H_0 - E)\psi_{AB,i} + H_2\psi_{DC,i} + H_3\psi_{DC,i-1} &= 0 \\ (H_0 - E)\psi_{DC,i} + H_2\psi_{AB,i} + H_3\psi_{AB,i-1} &= 0 \end{aligned} \quad (2.46)$$

Therefore, the amplitudes have been separated for each sublayer of each individual layer. Before proceeding, some important points regarding the amplitudes and energies of the $N-$layer BP system must be brought to attention. As discussed in the previous sections, the sub-Hamiltonians $H_k^{\pm}$ are associated with low (+) and high (-) energy bands near the Fermi level. This can be understood by analysing the eigenstates of each of these sub-Hamiltonians. For the monolayer case, the eigenstate Ψ_k^+ of the sub-Hamiltonian H_k^+ is given by the sum of the amplitudes of the equivalent sublattices for each component, that is, $\psi_{AB} + \psi_{DC}$, whereas the eigenstate Ψ_k^- is given by the difference of the amplitudes, i.e., $\psi_{AB} - \psi_{DC}$. Therefore, in analogy with the Hydrogen molecule, the bonding states are given by the sum of the individual wavefunctions (lowest energy) while the anti-bonding states are given by the difference of the individual wavefunctions (highest energy). Similarly, for the bilayer system, the Hamiltonian that describes the low energy bands has eigenstates that are bonding states. Likewise, the Hamiltonian that describes the high energy bands has eigenstates that are anti-bonding states. Differently from the single-layer case, though, the bilayer system allows for bonding and anti-bonding

between adjacent layers and not only in-between sublayers belonging to the same layer. In this case, the bonding states between different layers, that is, $[(\psi_{AB,1}+\psi_{DC,1})+(\psi_{AB,2}+\psi_{DC,2})]$ have lower energies than the anti-bonding ones, i.e., $[(\psi_{AB,1}+\psi_{DC,1})-(\psi_{AB,2}+\psi_{DC,2})]$. Therefore, four energy bands are expected: two of which are high energy and the other two are low energy. This was, of course, confirmed in the previous section. This argument can be extended to the multilayer system. The low energy bands are described by the bonding states of $\psi_{AB,i}$ and $\psi_{DC,i}$, that is, $\psi_{AB,i}+\psi_{DC,i}$ for each layer i and higher energy bands are described by the anti-bonding states $\psi_{AB,i}-\psi_{DC,i}$. The equations (2.46) can be rewritten in the basis of the bonding and anti-bonding states:

$$\begin{aligned}
(H_0 \pm H_2 - E)(\psi_{AB,1}+\psi_{DC,1}) + H_3\psi_{DC,1} &= 0,\\
(H_0 \pm H_2 - E)(\psi_{AB,2}+\psi_{DC,2}) + H_3(\psi_{DC,1} \pm \psi_{AB,1}) &= 0,\\
\vdots \qquad\qquad \vdots \qquad\qquad \vdots& \\
(H_0 \pm H_2 - E)(\psi_{AB,N}+\psi_{DC,N}) + H_3\psi_{AB,N} &= 0
\end{aligned} \tag{2.47}$$

The bonding and anti-bonding orbitals can be defined as $\phi_i^+ = \psi_{AB,i}+\psi_{DC,i}$ and $\phi_i^- = \psi_{AB,i}-\psi_{DC,i}$, respectively. In order to capture only the multilayer BP properties at low energy, the equations associated with the anti-bonding states can be discarded altogether, so only the half with a plus sign of equations (2.47) are used. Therefore, instead of having to diagonalize a $N\times N$ block Hamiltonian, one has to diagonalize a $N/2\times N/2$ effective block Hamiltonian.

In accordance to the symmetry between A/D and B/C sublattices, the following approximation is used:

$$\psi_{AB,i} \approx \psi_{DC,i}, \tag{2.48}$$

which corresponds to

$$\phi_{A,i} \approx \phi_{D,i} \text{ and } \quad \phi_{B,i} \approx \phi_{C,i}. \tag{2.49}$$

Consequently,

$$\psi_{AB,i} \approx \psi_{DC,i} \approx \frac{1}{2}\phi_i^+. \tag{2.50}$$

Within this approximation, the equations (2.47) become:

$$(H_0 + H_2 - E)\phi_i^+ + \frac{1}{2}H_3(\phi_{i-1}^+ + \phi_{i+1}^+) = 0, \tag{2.51}$$

with the boundary condition $\phi_0^+ = \phi_{N+1}^+ = 0$. This boundary condition is satisfied by the following *ansatz*: $\phi_j^+ = A\sin[jn\pi/(N+1)]$, where A is a two-component spinor that depends

on k_x, k_y only. Performing the sum ϕ^+_{i-1} and ϕ^+_{i+1}, one obtains:

$$\begin{aligned}\phi^+_{i-1} + \phi^+_{i+1} &= A\sin\left[\frac{n\pi(i-1)}{N+1}\right] + A\sin\left[\frac{n\pi(i+1)}{N+1}\right] \\ &= A\Big[\sin\left(\frac{n\pi j}{N+1}\right)\cos\left(\frac{n\pi}{N+1}\right) - \sin\left(\frac{n\pi}{N+1}\right)\cos\left(\frac{n\pi j}{N+1}\right) \\ &\quad + \sin\left(\frac{n\pi j}{N+1}\right)\cos\left(\frac{n\pi}{N+1}\right) + \sin\left(\frac{n\pi}{N+1}\right)\cos\left(\frac{n\pi j}{N+1}\right)\Big] \\ &= 2A\sin\left(\frac{n\pi j}{N+1}\right)\cos\left(\frac{n\pi}{N+1}\right) \\ &= 2\phi^+_i\cos\left(\frac{n\pi}{N+1}\right). \end{aligned} \tag{2.52}$$

Substituting the *ansatz* in equation (2.51),

$$\left[H_0 + H_2 + H_3\cos\left(\frac{n\pi}{N+1}\right)\right]\phi^+_i = E\phi^+_i, \tag{2.53}$$

where now $\phi^+_i = \phi^+_{i,n}(n = 1, 2, ..., N)$. Hence, the *ansatz* diagonalized the complete Hamiltonian of a BP multilayer system. The eigenvalues of the above Hamiltonian are:

$$\begin{aligned}E^{\pm}_{k,n} &= t_{AA}(k) + t_{AD}(k) + \cos\left(\frac{n\pi}{N+1}\right)t_{AD'}(k) \\ &\quad \pm \left|t_{AB}(k) + t_{AC}(k) + \cos\left(\frac{n\pi}{N+1}\right)t_{AC'}(k)\right|. \end{aligned} \tag{2.54}$$

The energy gap for a $N-$layer system can be obtained by setting $k = 0$ in the above equation:

$$E^N_g = 2\left|t_{AB}(0) + t_{AC}(0) + \cos\left(\frac{N\pi}{N+1}\right)t_{AC'}(0)\right|, \tag{2.55}$$

where the states with $n = N$ are the ones with lowest energies. Noting the parity of the cosine function and also that $E^{\text{mono}}_g = 2|t_{AB}(0) + t_{AC}(0)|$, the equation above can be rewritten as:

$$E^N_g = \left|E^{\text{mono}}_g - 2\cos\left(\frac{\pi}{N+1}\right)t_{AC'}(0)\right|. \tag{2.56}$$

The energy gap for bulk BP is obtained by letting $N \to \infty$, by which one finds that $E^{\text{bulk}}_g = 0.414$ eV.

3 DIRAC CONES IN PHOSPHORENE

The energy gap of multilayer phosphorene systems can be tuned through the application of an external perpendicular electric field. Such a mechanism induces a topological phase transition for fields at the vicinity of a critical value D_c for which a gap closure is achieved. For fields lower than D_c, the familiar anisotropic dispersion is observed with slightly different effective masses, whereas the formation of Dirac cones is observed for fields above that critical value. In this chapter, the band structure of bilayer BP will be obtained by the tight-binding Hamiltonian demonstrated in the previous section, now incorporating an approximated unscreened electric field effect, showing how the bands change under its effect, eventually leading to the topological phase transition. Next, an investigation of the effects of the topological phase transition on the carrier concentrations of the system is made within the same approximation. Finally, an analogous calculation is made for phosphorene nanoribbons followed by a scheme to assess the edge orientation and size of the system based on scaling laws.

3.1 Electrostatics of the problem

An intuitive way of incorporating the bare electric field into the TB Hamiltonian is by changing the on-site energies in order to reflect the influence of an electrostatic potential. From fundamental electrostatics, the electric field between two infinitely large plates with opposite surface charge densities (σ and $-\sigma$) is given by:

$$F_0 = \frac{\sigma}{\kappa\epsilon_0} = \frac{en_g}{\kappa\epsilon_0}, \tag{3.1}$$

where n_g is the gate density, e is the fundamental electronic charge, ϵ_0 is the vacuum permittivity and κ is the dielectric constant of the medium. The field is therefore constant between the two plates and zero elsewhere, as seen in Fig. 14. In a single layer of phosphorene, the atoms are arranged into two sublayers. Therefore, there will be an energetic asymmetry between atoms belonging to sublattices in different sublayers, which is calculated as:

$$\Delta_{i,i+1}(n_g) = \frac{e^2 n_g}{\kappa\epsilon_0} d_{i,i+1}, \tag{3.2}$$

where $d_{1,2} = d_{3,4} = d_{intra}$ and $d_{2,3} = d_{inter}$ $(i = 1, 2, 3)$. Finally, setting the zero of potential energy at the uppermost sublayer, the total electrostatic energy in each sublayer is given by:

$$U_j = 0 \quad (j = 1); \quad U_j = \sum_{i=1}^{j-1} \Delta_{i,i+1}(n_g)(i > 1). \tag{3.3}$$

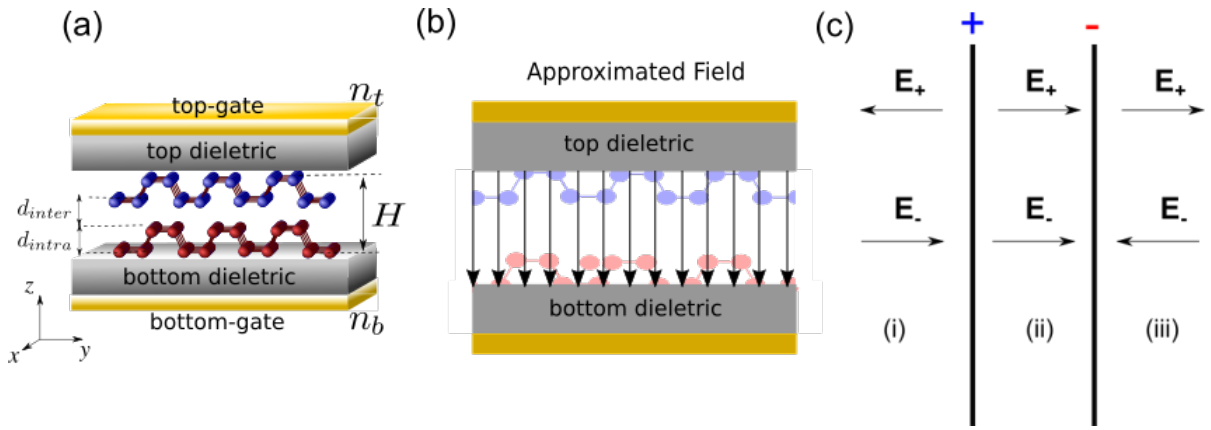

Figure 14: (a) Schematic representation of the system, showing a bilayer phosphorene film between a top and a bottom gate, with electronic gate densities $n_g = n_t = -n_b$. (b) Approximated bare electric field used in this problem. (c)Representation of electric field produced by two parallel infinite plates. The field lines point outwards from the positive plate and inwards to the negative one, reinforcing each other in between the plates (region i) and cancelling elsewhere (regions ii and iii).

These terms are then added to the ith sublayer on-site elements of the bilayer TB Hamiltonian, which will be used as a prototype of multilayer phosphorene:

$$\mathcal{H}_{bi} = \begin{pmatrix} H + V_1 & H_c \\ H_c^\dagger & H + V_2 \end{pmatrix}, \tag{3.4}$$

where

$$V_1 = \begin{pmatrix} U_1 & 0 \\ 0 & U_2 \end{pmatrix}, \quad \text{and} \quad V_2 = \begin{pmatrix} U_3 & 0 \\ 0 & U_4 \end{pmatrix}. \tag{3.5}$$

The sub-Hamiltonians H and H_c correspond to the monoloayer and interlayer coupling terms, respectively, and have been defined in the previous chapter.

3.2 Multilayer Phosphorene

3.2.1 Electronic Structure

The energy bands are obtained by diagonalizing the corresponding Hamiltonian (3.4) for three different cases: below, at and above a critical gate density value n_c associated with a critical perpendicular field D_c. Each one of these cases represents a distinct phase of the system. For unbiased BP ($n_g = 0$), the band structure corresponds to an anisotropic, direct-gap semiconductor, with the energy gap located at the Γ point of the Brillouin zone. In the presence of an external perpendicular bias ($0 < n_g < n_c$), the dispersion is slightly deformed and the energy gap is continuously reduced. The bands move closer to each other with increasing gate densities ($n_g = n_c$) and eventually the system becomes gapless. At this point, the material transitions from a semiconducting to a semi-metallic phase. The gate density required to close the gap is $\sim 10.2 \times 10^{13}$ cm^{-2}. For even higher gate densities ($n_g > n_c$), an inversion of the

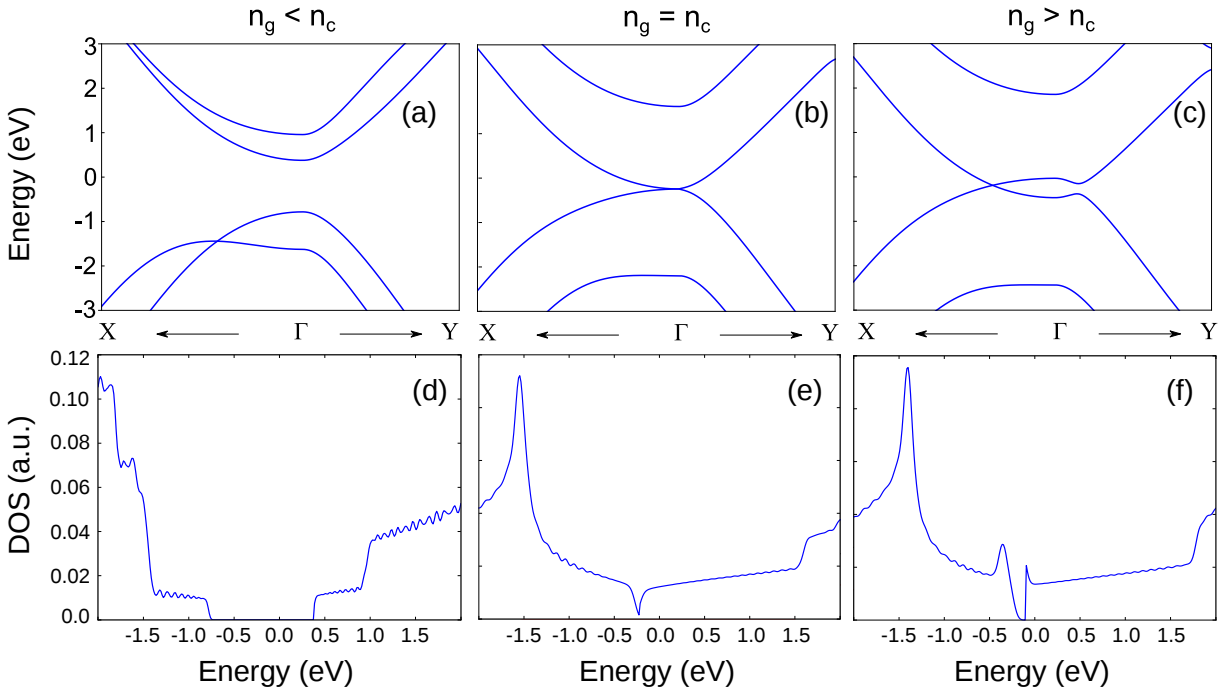

Figure 15: (a)-(c) Band structure and (d)-(f) DOS of a bilayer phosphorene system under a continuously increasing gating potential. The critical gate density is $\sim 10.2 \times 10^{13}$ cm^{-2}.

bands takes place with the characteristic emergence of a Dirac cone along the $\Gamma \rightarrow X$ direction.

The density of states (DOS) can also be used to visualize the topological phase transition. Formally, it is defined as:

$$d(E) = \int_{BZ} \frac{\mathbf{dk}}{4\pi^2} \delta(E - E(\mathbf{k})), \tag{3.6}$$

where $\delta(E - E(\mathbf{k})$ is the Dirac delta function and the integration is performed over the Brillouin zone. In this work, it was numerically calculated using a Gaussian function as an approximation of the Dirac delta:

$$\delta(E - E_0) \approx f(E) = e^{-(E-E_0)^2/\Gamma^2}, \tag{3.7}$$

where $\Gamma = 0.05$ is the broadening factor. For $n_g < n_c$, it presents the typical behavior of a gapped system, with an energy gap perfectly matching the band structure. At $n_g = n_c$, the DOS turns into that of a semimetallic material, with a small but finite number of states at the energetic region where the bands touch. For $n_g > n_c$, however, its behavior changes considerably at the vicinity of the transition point. In this region, the shape of the DOS resembles that of graphene, which is further evidence of the linear band dispersion [67].

In contrast with multilayer systems, the monolayer band gap can never be closed through external gating. In fact, a continued opening of the gap takes place for increase values of gate density. This result can be demonstrated mathematically using a simplified TB model

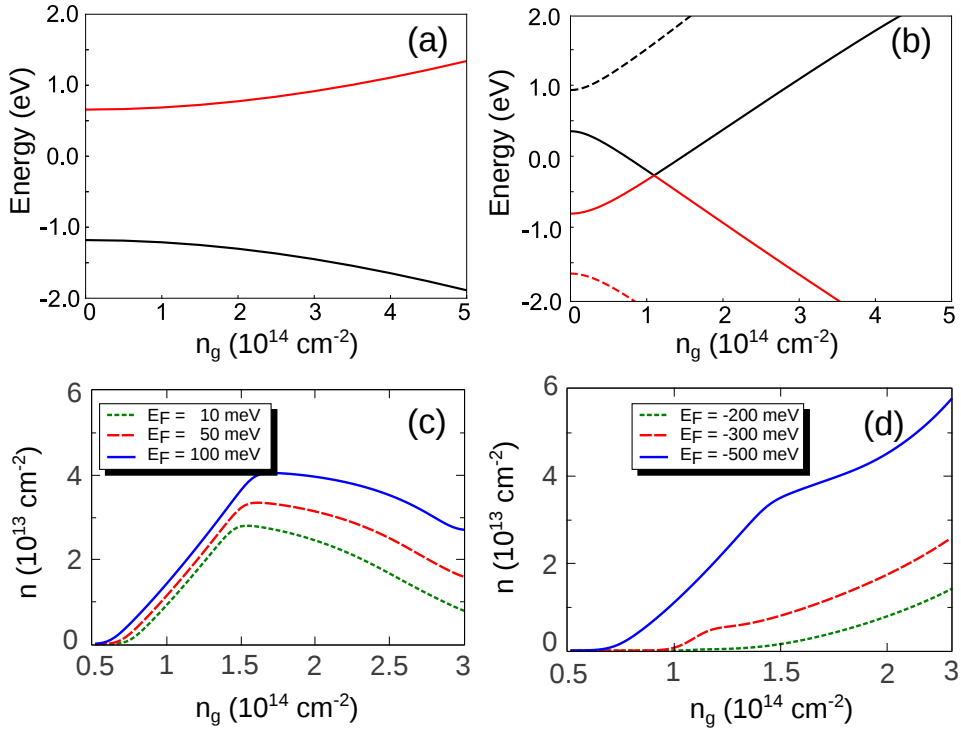

Figure 16: Conduction and valence band edges as a function of n_g for (a) monolayer and (b) bilayer phosphorene. Whereas the gap closes for a bilayer system, it continually increases for the monolayer case. Carrier concentration as a function of the gate density for various Fermi levels at (c) the conduction band, for electrons and (d) the valence band, for holes.

including the leading hopping terms with an on-site potential energy Δ ($-\Delta$) simulating the effect of the electric field. It can be shown that, for the monolayer case, there will never be a solution for Δ that will make the energy gap vanish [51]. Such mathematical demonstration is beyond the scope of this work, but the variation of the energy gap was calculated here numerically by using the full TB model presented in the previous chapter and the results can be seen in Fig. 16 (a). For the bilayer, the closing of the gap is readily seen at some critical value n_c.

3.2.2 Carrier Concentration

Such a variation of the density of states in the vicinity of the Dirac cones suggests that the carrier concentration of the system would present a similarly peculiar behaviour. The concentrations for electrons and holes are thus calculated using the following formulas:

$$\begin{aligned} n &= 2\iint dk_x dk_y f_{CB}(E(\mathbf{k}) - E_F) \\ h &= 2\iint dk_x dk_y [1 - f_{VB}(E(\mathbf{k}) - E_F)], \end{aligned} \tag{3.8}$$

where f_{CB} and f_{VB} are the Fermi-Dirac distributions associated with the conduction and valence bands, respectively. The factor of 2 is due to the spin degree of freedom. It is important to emphasize that this model works within the approximation of an unscreened electric field

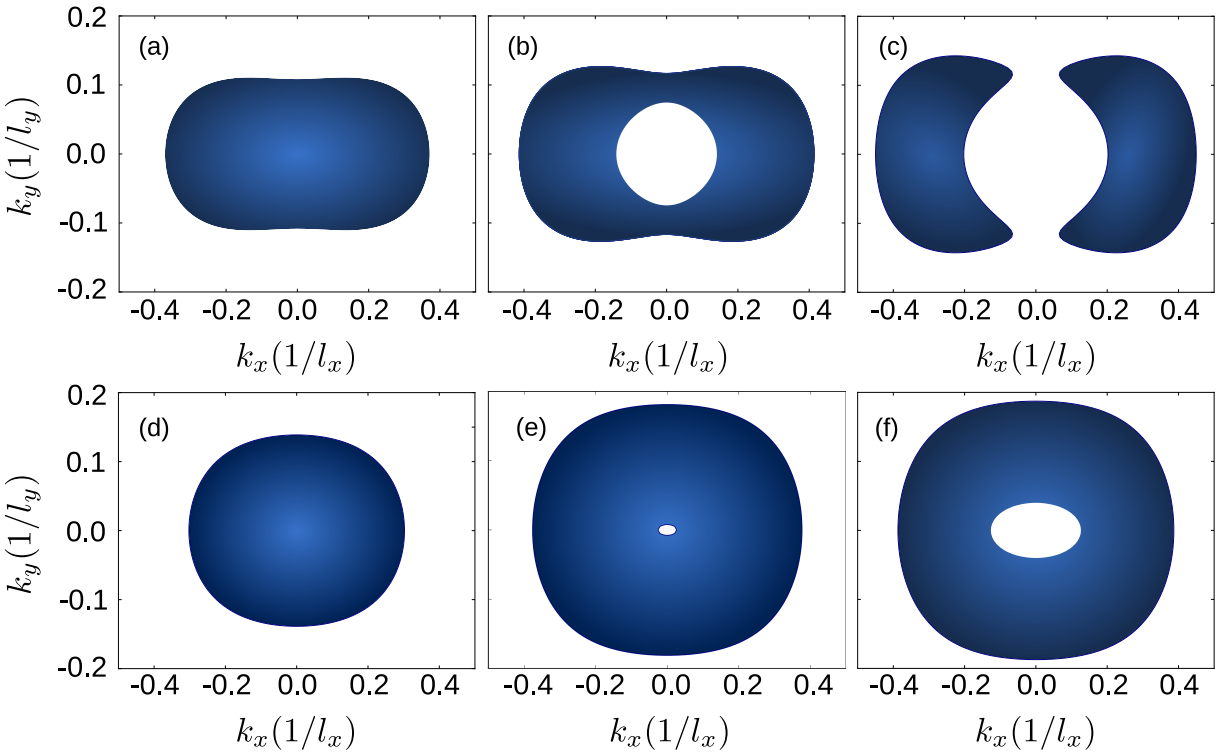

Figure 17: Evolution of the Fermi surface with increasing values of n_g, for two different pinned Fermi levels: (a)-(c), the Fermi level is at $E_F = 400$ meV, at the conduction band for the entirety of this process and (d)-(f) for $E_F = -10$ meV, at the valence band. All gate densities in this calculation are above n_c.

with a constant Fermi level. A proper way to obtain the correct expressions for the gate induced carrier density of multilayer phosphorene will be addressed in the final chapter.

The pinning of the Fermi level allows for a solid to assume $n-$type or $p-$type behavior under external gating. If the system behaves like a $n-$type semiconductor, the Fermi level intercepts the conduction band, whereas it intercepts the valence band for $p-$type behavior. As seen in the previous section, the valence band edge is raised in energy while the conduction band edge has its energy lowered in the presence of external gating. Therefore, if the Fermi level is pinned closer to the conduction band, the electron concentration increases with n_g. Such increase happens up to and beyond the point of transition, reaching a maximum near the stage where the inverted conduction band touches the Fermi level. This behavior can be seen in Fig. 16 (c) for three different Fermi levels, respectively pinned at 10 meV, 50 meV and 100 meV. As seen in the figure, the point at which the maximum occurs varies, of course, with the chosen Fermi level. Beyond this point, the topology of the Fermi surface is effectively altered, as shown in Fig 17(a)-(c). This transition results in the decrease of the electron concentration of the system, as seen in Fig. 16 (c).

When the Fermi level is fixed near the valence band, the system behaves like a $p-$type semiconductor. Therefore, the hole concentration in the system also increases, as shown in Fig. 16 (d). However, at the point of band inversion, this rising is attenuated by the band

inversion at $n_g > n_c$, which again results in a topological change of the Fermi surface, as is made evident in Figs. 17 (d)-(e). Contrary to the electron concentration behavior, however, the hole concentration does not decrease for gate densities in the vicinity of n_c. This is because the tearing of the Fermi surface is compensated by its increase in area. Such an asymmetric result is likely a result of the anisotropic properties of phosphorene. It is possible that the concentration of holes would start to decrease at some point, but not for values of n_g quite beyond the ones used in this calculation.

Whether or not this could actually happen in an experimental situation is a matter of a more careful study taking into account the effects of screening and also the Fermi level adaptation to the new deformed bands.

3.3 Nanoribbons

In this section, I tackle the emergence of Dirac cones in a phosphorene nanoribbons (PNRs). Much like the previous sections, the band structure and DOS are calculated for varying quantities of n_g in order to see how the topological phase transition would look like in the presence of lateral confinement. Following the same progression of the previous section, a study of the carrier concentration dependence on the gate density is made. Finally, a scheme to assess the edge orientation and width of the nanoribbons is proposed based on the carrier concentration behavior.

The theoretical framework is the same as the one described in the previous section. In addition to the unscreened field approximation, the effects of the bending of the field lines at the edges of the nanoribbons are also dismissed. As a prototype for multilayer systems, we consider nanoribbons with zigazg (zz) and armchair (ac) edges. The zz (ac) nanoribbon is oriented along the x (y) axis, being limited by its width W along the y (x) direction and by its thickness H along the z direction, as skecthed in Fig. 18(a). The thickness is related to the number of layers N by $H = d_{intra}N + d_{inter}(N-1)$, where $d_{intra} = 2.153$ Å and $d_{inter} = 3.214$ Å are the intralayer and interlayer distances, respectively. The tight-binding calculations in this section were performed by using the KWANT Python package [68].

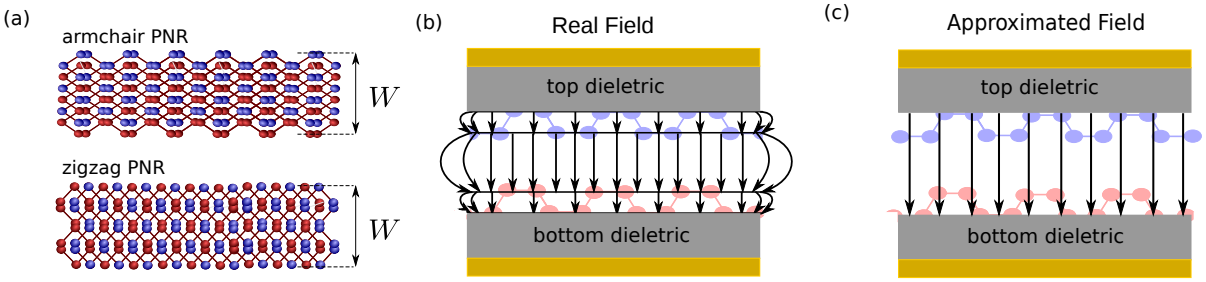

Figure 18: (a) Top view of armchair (top panel) and zigzag (lower panel) BP nanoribbons with width W. A sketch of the real and the approximated screened electric field is presented in (b) and (c), respectively.

3.3.1 Band structure and Density of States

We start by investigating the behavior of the energy dispersion of PNRs under the influence of gate voltages. We consider the case of bilayer BP nanoribbons in our calculations. Initially, we consider ribbons with fixed width $W = 20$ nm and assume that the charge concentrations on the top and bottom gates (n_t and n_b, respectively) have equal absolute values, but with opposite signs $n_t = -n_b = n_g$. Figure 19 shows the energy bands and the respective DOS for zigzag (a)-(c) and armchair (d)-(f) BP nanoribbons with different values of n_g. The critical density for zz and ac nanoribbons, $n_c^{zz} = 11.37 \times 10^{13}$ cm^{-2} and $n_c^{ac} = 11.17 \times 10^{13}$ cm^{-2}, respectively, generates critical displacement fields, D_c^{zz} and D_c^{ac}, for which a gap closure is achieved. As expected, the value of n_c required to close the gap is higher for nanoribbons due to the confinement effects. For densities lower than $n_c^{zz(ac)}$ one observes the typical anisotropic parabolic energy dispersion of phosphorene systems, which leads to nanoribbons with different band curvatures, as one can see in Figs. 19(a) and (d). Additionally, the DOS also presents the typical behavior of gapped systems, showing more pronounced peaks for the zz case than for the ac case. This is due to the smaller band curvature in the zz case, which results in a wider range of momenta in which Van Hove singularities happen. In other words, re-writing the DOS as:

$$d(E) = \int_{\Omega} \frac{\mathbf{dk}}{4\pi^2} \frac{1}{|\nabla E_{\mathbf{k}}|}, \tag{3.9}$$

where Ω is a surface of constant energy. The gradient of the energy approaches zero as the energy approaches a minima. Therefore, the DOS diverges. At the critical density, a gap closure is observed as one can see in Figs. 19(b) and (e) for zz and ac bilayer PNRs, respectively. One can notice that the conduction and valence bands touch without any significant distortion of the parabolic behavior of the dispersion.

For densities greater than $n_g^{zz(ac)}$, the valence and conduction bands undergo a phase transition resulting in the formation of Dirac-like spectra. Such behavior can be seen in Fig. 19(c) and (f) for the zz and the ac cases, respectively. For sufficiently low energies in both cases, the dispersion resembles those of graphene nanoribbons, in which one observes the presence of two Dirac cones in the zz case and a single point in which the dispersion is approximately linear in the ac case [69, 66]. Additionally, zz graphene nanoribbons have flat bands corresponding to states localized at the edges of the ribbons. However, in the case of gated zz phosphorene nanoribbons the quasi-flat bands that appear between the two quasi-Dirac cones are not related to states localized at the edges of the ribbon, since we are considering ribbons that do not support edge states (beard zz nanoribbons [70, 71]). Interestingly, the DOS has a complicated structure, showing a great asymmetry between the new conductance and valence bands at low energies. This behavior resembles those of massless Dirac Fermions in graphene

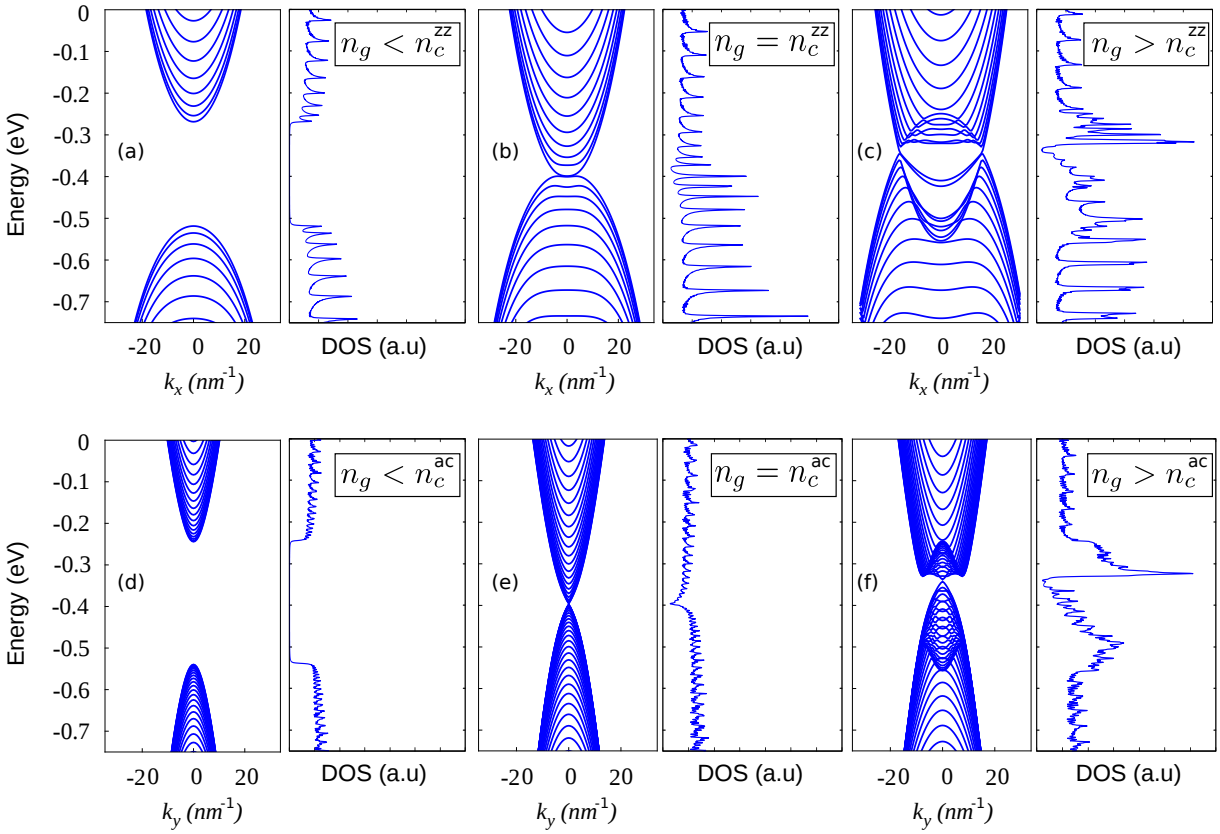

Figure 19: Dispersion relation and the correspondent density of states for (a)-(c) zigzag and (d)-(f) armchair phosphorene nanoribbons with various values of n_g, for a unscreened electric field. Three different situations are considered: (a) and (d), $n_g < n_c^{zz}$ ($n_g < n_c^{ac}$), (b) and (e) $n_g = n_c^{zz}$ ($n_g = n_c^{ac}$), (c) and (f) $n_g > n_c^{zz}$ ($n_g > n_c^{ac}$), where n_g^{zz} (n_g^{ac}) is the critical gate density for which a gap closure is achieved. The values of gate densities used for these calculations, in units of $10^13 cm^{-2}$, where: 9.37, 11.37 and 13.37 for (a), (b) and (c) and 9.17, 11.17 and 13.17 for (d), (e) and (f), respectively.

[69], reinforcing the linear nature of the dispersion in BP at low energies for densities greater than the critical one.

3.3.2 Carrier concentration

Similarly to the infinite sheet, the great variation of the DOS at the transition suggests that one can achieve significant modulation of the carrier concentration, at a low Fermi level, with a small variation in the gate carrier density. Therefore, the the carrier concentration is calculated using the following equation:

$$n = 2\sum_{k,n} f(E_{k,n} - E_F), \tag{3.10}$$

where $f(E_{k,n} - E_F)$ is the Fermi-Dirac distribution, $E_{k,n}$ is the dispersion of the nth mode and E_F is the Fermi level. The factor of 2 is due to the spin degeneracy. Figs. 20(a) and (b) show the dependence of this quantity as function of the gate density for zz and ac bilayer phosphorene nanoribbons, respectively, considering different Fermi levels $E_F = E_i$ (with $E_1 =$

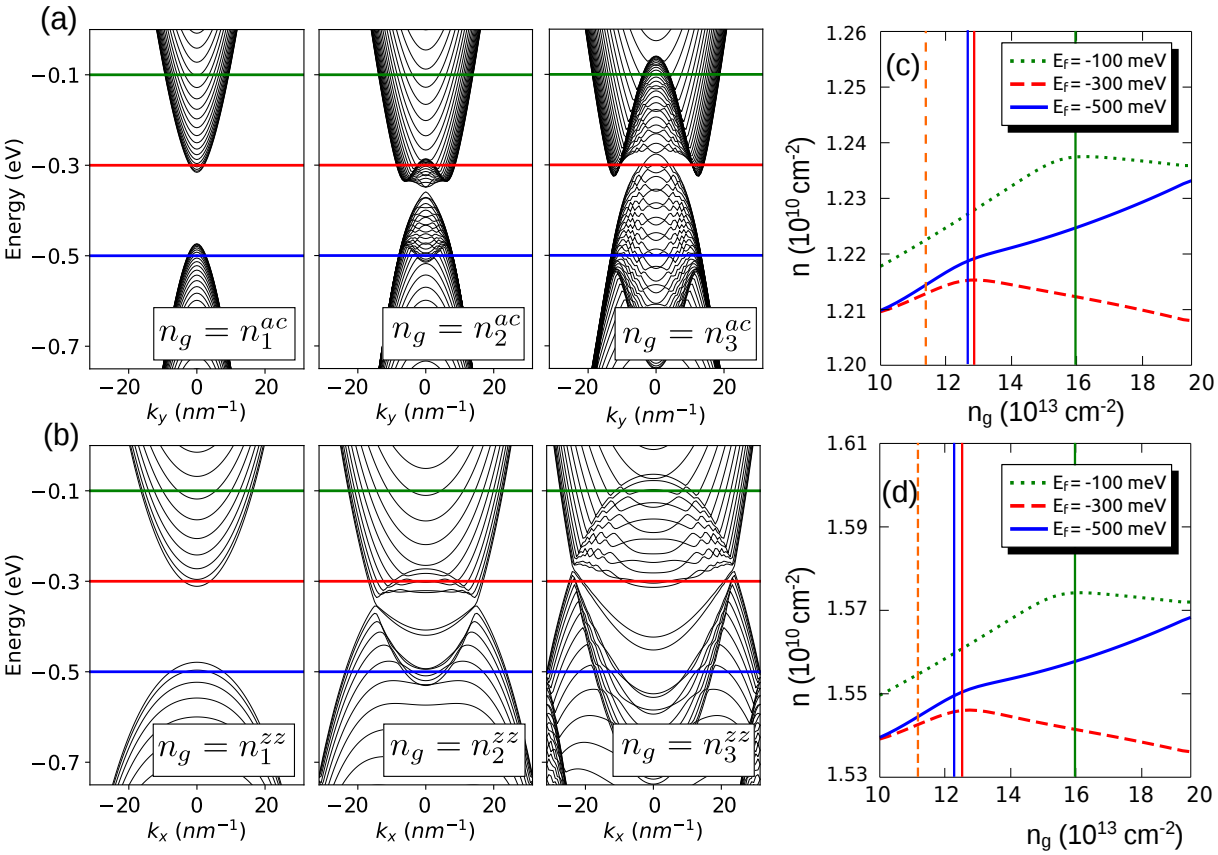

Figure 20: Carrier concentration n as a function of the gate density at different Fermi levels for (a) zz and (b) ac bilayer phosphorene nanoribbons. The vertical orange dashed lines mark the critical densties for each case : $n_c^{zz} = 11.37 \times 10^{13}$ cm^{-2} and $n_c^{ac} = 11.17 \times 10^{13}$ cm^{-2} for zz and ac ribbons, respectively. The other vertical lines mark the transition gate densities. Thus, $n_1^{zz(ac)}$, $n_2^{zz(ac)}$ and $n_3^{zz(ac)}$ are the mentioned densities for the Fermi levels $E_F = -500$ meV, $E_F = -300$ meV and $E_F = -100$ meV, respectively. Figures (c) and (d) show the band structure for the zz and ac cases, respectively, considering the transition gate densities mentioned above. The horizontal lines in these figures mark the Fermi levels considered in this analysis.

-500 meV, $E_2 = -300$ meV and $E_3 = -100$ meV), at $T = 300$ K. In each figure, the orange vertical dashed line marks the position of the critical gate densities. Considering $E_F = E_3$ and $E_F = E_2$, one notices an increase in the carrier concentration even for gate densities greater than $n_c^{zz(ac)}$, as one can see from the dotted green and dashed red curves in both figures. For $E_F = E_1$, one observes a decrease in the carrier concentration of the ribbons. This is due to the fact that the Fermi level is at the valence band region in the latter case, leading to an excess of positive charge carriers in the system (p-type behaviour). The the Fermi levels $E_F = E_2$ and $E_F = E_3$ are in the conduction band region, corresponding to an excess of negative charge carriers (n-type behaviour). Therefore, it is natural to expect that the carrier concentration would increase with the gate density for both systems, similarly to the infinite case. However, for certain values of n_g (n_i^{ac} and n_i^{zz} for zigzag and armchair PNRs, where i is associated with the Fermi level), the concentration of electrons starts to decrease, while the concentration of holes starts to increase at a slower pace, as seen in Figs. 20(a) and (b). The gate densities for

which the transition occurs are $n_2^{zz} = 12.50 \times 10^{13}$ cm^{-2} ($n_2^{ac} = 12.75 \times 10^{13}$ cm^{-2}) and $n_3^{zz} = 16.25 \times 10^{13}$ cm^{-2} ($n_3^{ac} = 16.00 \times 10^{13}$ cm^{-2}) for the zigzag (armchair) PNRs.

Such behavior is a unique characteristic of the phase transition, which allows for a change in the sign of the curvature of a band for a range of momenta at the vicinity of the Γ point. At the conduction (valence) band, a subband with negative (positive) effective mass contributes as hole (electron) bands. Therefore, an excess of positive (negative) charge carriers is added to the negative (positive) excess carrier density of a *n*-type (*p*-type) system. For a given Fermi level in the *n*-type case, the electrons concentration will slow down and come to a hault whenever the top of the hole subbands touches the Fermi level. Consequently, as the contribution of the holes bands becomes more pronounced than the electron bands, the carrier concentration will start to decrease. In fact, Figs. 20(c) and (d) show the energy dispersion for the ac and zz nanoribbons, respectively, considering the corresponding gate densities for which the carrier concentration starts to decrease for a given Fermi level. The horizontal lines mark the positions of the assumed Fermi levels : $E_F = E_1$ (blue curve), $E_F = E_2$ (red curve) and $E_F = E_3$ (green curve). As one can notice in the case of the *n*-type BP nanoribbons, for densities greater than $n_c^{zz(ac)}$, there are several energy subbands at the conduction band in which the curvatures are negative. More specifically, for $n_g = n_2^{zz(ac)}$ these subbands start to touch the Fermi level $E_F = E_2$. A similar behavior is observed for the transition gate density $n_3^{zz(ac)}$ and the Fermi level $E_F = E_3$, which is consistent with the non-monotonic behavior of the carrier concentration.

3.3.3 Scaling laws

The properties discussed so far also hold for phosphorene nanoribbons with arbitrary widths and thicknesses. In fact, one can always find a transition gate density $n_i^{zz(ac)}$, for a given Fermi level, for zz and ac PNRs for several different sizes. Figure 21(a) shows the behavior of the gate density $n_3^{zz(ac)}$ ($E_F = E_3$) for bilayer PNRs with several widths. The symbols are the tight-binding results, where the red circles (blue triangles) correspond to the ac (zz) case, and the solid curves are the fittings. As seen, there is a drop in the value of the transition gate densities with W and despite the difference in the values of n_3 for zz and ac cases, the scaling behavior is the same for both cases. The best fit shows a $\propto W^{-2}$ behavior that is quite distinct from what one would expect, since other properties, such as the energy gap of PNRs, present different scaling laws due to the differences in the momentum dependency of the energy levels in the x and y directions[70]. A similar picture holds true for the dependence of $n_3^{zz(ac)}$ with the thickness of the ribbons, i.e. with the number of layers N. In figure 21(b), we show the transition gate density for the chosen Fermi level as a function of the number of layers for a fixed width $W = 20$ nm. For such wide ribbons, the n_3 values for zz and ac ribbons are very

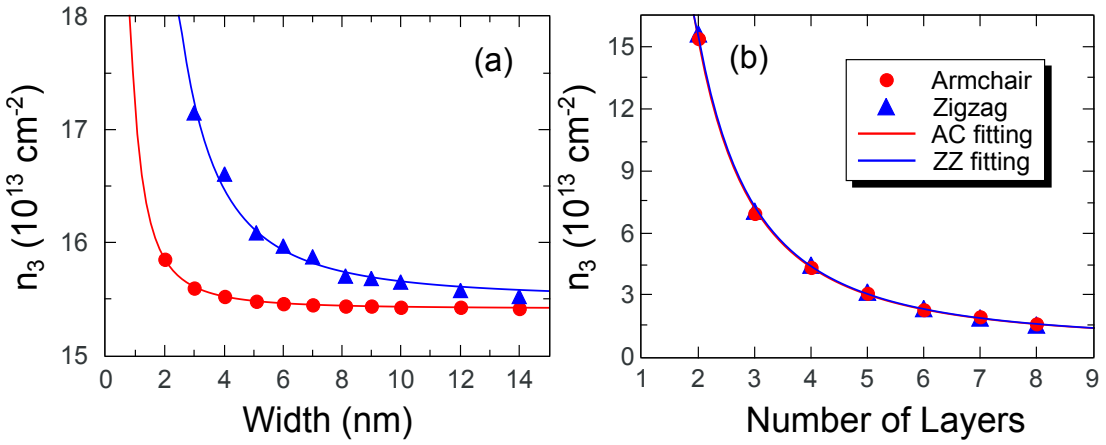

Figure 21: (a) Width dependence of the gate density $n_3^{zz(ac)}$ for zigzag (blue results) and armchair (red results) bilayer BP nanoribbons. (b) Thickness dependence of nanoribbons with fixed width $W = 20nm$. The symbols are the results obtained from the tight-binding model, whereas the solid curves are the correspondent fittings.

close to each other. The result shows a clear decrease in n_3 for both cases, exhibiting a N^{-2} behavior as in the case of the width dependence.

The present results suggest a scheme by which one may assess width and the thickness of phosphorene systems: The specific values of the transition gate densities $n_i^{zz(ac)}$ can be detected experimentaly through Hall measurements at low magnetic fields. As shown, a small change in n_g beyond $n_i^{zz(ac)}$ causes the carrier concentration to decrease for *n*-doped BP nanoribbons. In this way, the obtained result can be compared with the values of Fig. 21, determining the corresponding width and thickness. We expect such method to be accurate for ribbons with small dimensions, since the values of $n_i^{zz(ac)}$ are very close for larger systems.

It is important to emphasize that the previous results are based on the assumption of an unscreened electric field. In a realistic setting, the charge distribution inside multilayer BP systems generate an electric field that counteracts the previous one, resulting in a screened field. Such an effect plays an important role in the determination of the specific values of the gate critical densities[63].

4 CONCLUDING REMARKS

In summary, we have studied the electronic properties of phosphorene in single and multilayer form by use of a tight-binding method. The method was applied to study the topological phase transition that is induced via the application of an external perpendicular bias. The strength of the bias was controlled by the number of carriers in the gate, namely, the gate density n_g. Increasing the strength of the bias slowly deforms the bands and eventually closes the gap at some critical value n_c, turning the material into a semi-metal. For even higher values of n_g, Dirac cones emerge in the spectrum of phosphorene, caused by the inversion of the conduction and valence bands, which makes phosphorene a Dirac semi-metal in this regime. The effects of this phase transition on the carrier concentration of phosphorene systems, including nanoribbons with zigzag and armchair edges, was studied. Our model is based on an approximated unscreened field which incorporates the electrostatic energy provided by the gates by changing suitably the on-site energy terms on the Hamiltonian.

Our findings indicate that the electron and hole concentration are greatly affected by the appearance of the Dirac cones, where the former starts to decrease at the point where the inverted conduction band touches the Fermi surface, effectively opening a hole in it and the latter is attenuated by the valence band inversion. Such effect was observed for the infinite system and nanoribbons alike. The gate density for which the inverted bands touched the Fermi surface is called transition concentration and is denoted in this work by n_i (where i stands for a particular pinned Fermi level, not to be confused n_c). We studied how this transition concentration changes with (a) the width of a phosphorene nanoribbon with a fixed number of layers and (b) the number of layers with a fixed width. Our results show that, for both zigzag and armchair nanoribbons, $n_i \sim 1/W^2$, where W is the width of the ribbon. The scaling factor differs for both types of nanoribbons, which suggests that such mechanism can be used to assess the edge orientation of the ribbons. Furthermore, we found that $n_i \sim 1/N^2$, where N is the number of layers. The proportionality is the same for zigzag and armchair nanoribbons, provided that they are sufficiently large. This can presumably be used to assess the number of layers in a phosphorene sample.

It is important, however, to emphasize the limitations of the description employed here. In general, the effects of screening cannot simply be ignored in a problem like this. The external bias induces charge concentrations on the phosphorene sublayers, which in turn create a counter-acting field that opposes the bare electric field from the gates. The induced charge

concentration can be calculated from a formula like the one shown below:

$$n = 2\sum_{\mathbf{k}} f[E(\mathbf{k})](|\phi_X^{(i)}|^2 + |\phi_Y^{(i)}|^2), \tag{4.1}$$

where $\phi_X^{(i)}$ and $\phi_Y^{(i)}$ are the probability amplitudes that the electron or hole will be found at the sublattices X and Y, respectively, which are both in the same sublayer i. On the other hand, the Hamiltonian should therefore depend also on this induced charge concentration, which are not known in advance. Therefore, a self-consistent Hartree approximation could be implemented into this TB model in order to find the correct induced charge concentrations. One would have to guess an initial concentration for each sublattice, diagonalize the Hamiltonian to find the bands, canculate the new carrier concentrations from Eq. 4.1, which would then be re-used to calculate the Hamiltonian and so on, until convergence is reached. The variation of the Fermi level also has to be taken into account more carefully. This will be the topic for new studies in the near future.

Despite the shortcomings of the model used here, however, we believe it served as a good application of the tight-binding method and it hopefully can predict to some degree what will happen in a more detailed calculation.

A CALCULATION OF THE HOPPING VECTORS AND STRUCTURE FACTORS

In this section, I will calculate the structure factors of the 10-hopping TB model. One needs the hopping vectors in order to calculate the structure factors. As a reminder, the hopping vector is the vector $\mathbf{r}_i - \mathbf{r}_j$ from an origin atom to another at a fixed sublatticea target at a fixed sublattice. In this calculation, the origin atom will be at the sublattice A. As seen in Fig. 22 (a), the bond in-plane bond angle is α_1 and the out-of-plane ones are α_2 and β. The bond angles are a_1 and a_2, respectively, for in-plane and out-of-plane bonds. The in- and intra-layer hopping paramaters are shown in Figs. 22 (b) and (c).

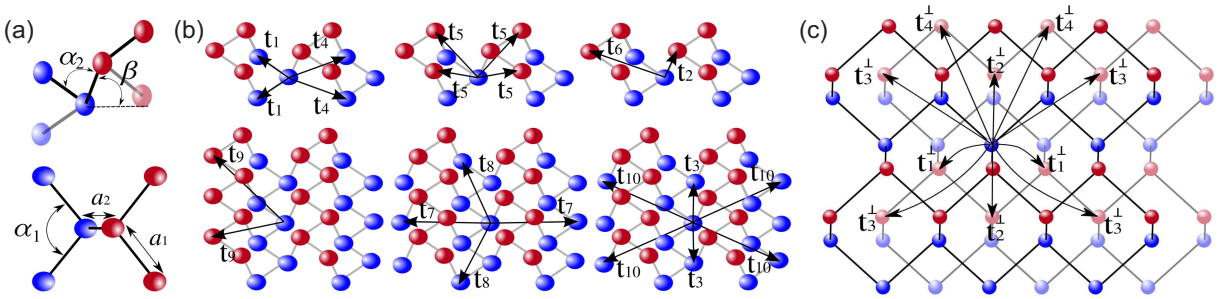

Figure 22: Crystal structure of BP phosphorene, highlighting the hopping parameters used in the TB-model. (a) Definition of the bond lengths and angles. (b) and (c) illustrate schematically the inter- and intra-layer hopping marameters, respectively. Figure extracted from Ref. [61]

An electron at a given atom of the sublattice A can hop to eight other atoms at the same sublattice: two with associated hopping paramater t_3, two with t_7 and four with t_{10}. Therefore, there will be 8 hopping vectors connecting the origin site to each of the target sites. Similarly, it may hop to two atoms at the sublattice B via t_1, two via t_4 and two via t_8. From A to C, it can hop to one with t_2, to one with t_6 and to two with t_9. Finally, it can hop from A to D to two atoms with t_5. Given the orientation of the axes x and y and the bond angles and lengths, it is easy to obtain the components of the hopping vectors.

A.1 From A to A

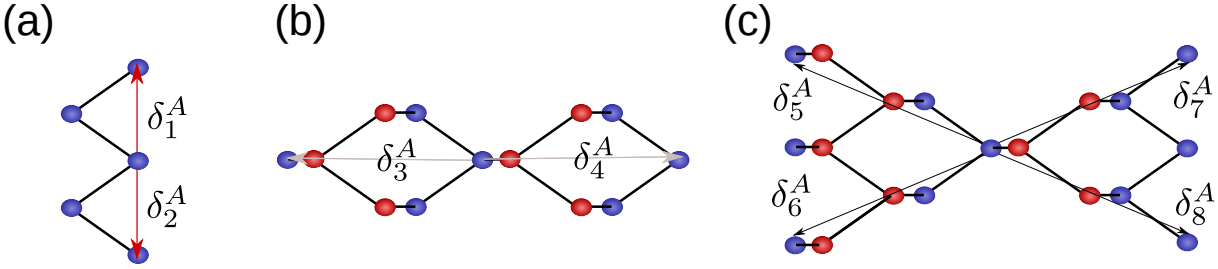

Figure 23: Hopping vectors form an origin site at A to a target site at A.

The hopping vectors with associated hopping paramaters t_3 are:

$$\delta_1^A = -2a_1 \sin(\alpha_1/2)\hat{\mathbf{x}},$$
$$\delta_2^A = 2a_1 \sin(\alpha_1/2)\hat{\mathbf{x}}. \tag{A.1}$$

The ones associated with t_7 are:

$$\delta_3^A = -(2a_1 \cos(\alpha_1/2) + 2a_2 \cos\beta)\hat{\mathbf{y}},$$
$$\delta_4^A = (2a_1 \cos(\alpha_1/2) + 2a_2 \cos\beta)\hat{\mathbf{y}}. \tag{A.2}$$

It's easy to see from the first image that the first two and the last two are in the $\hat{\mathbf{x}}$ and $\hat{\mathbf{y}}$ directions, respectively. Finally, the hopping vectors associated with t_{10} are:

$$\begin{aligned}
\delta_5^A &= -2a_1 \sin(\alpha_1/2)\hat{\mathbf{x}} - 2(a_1 \cos(\alpha_1/2) + a_2 \cos\beta)\hat{\mathbf{y}} \\
\delta_6^A &= 2a_1 \sin(\alpha_1/2)\hat{\mathbf{x}} - 2(a_1 \cos(\alpha_1/2) + a_2 \cos\beta)\hat{\mathbf{y}} \\
\delta_7^A &= -2a_1 \sin(\alpha_1/2)\hat{\mathbf{x}} + 2(a_1 \cos(\alpha_1/2) + a_2 \cos\beta)\hat{\mathbf{y}} \\
\delta_8^A &= 2a_1 \sin(\alpha_1/2)\hat{\mathbf{x}} + 2(a_1 \cos(\alpha_1/2) + a_2 \cos\beta)\hat{\mathbf{y}}.
\end{aligned} \tag{A.3}$$

Therefore, the structure factor $t_{AA}(k)$ is given by:

$$\begin{aligned}
t_{AA}(k) = t_3[&e^{ik_x 2a_1 \sin(\alpha_1/2)} + e^{-ik_x 2a_1 \sin(\alpha_1/2)}] \\
&+ t_7[e^{i2k_y(a_1 \cos(\alpha_1/2)+a_2 \cos\beta))} + e^{-i2k_y(a_1 \cos(\alpha_1/2)+a_2 \cos\beta))}] \\
&+ t_{10}[e^{-i2a_1 \sin(\alpha_1)k_x}(e^{2i(a_1 \cos(\alpha_1/2)+a_2 \cos\beta)} + e^{-2i(a_1 \cos(\alpha_1/2)+a_2 \cos\beta)}) \\
&+ e^{-i2a_1 \sin(\alpha_1)k_x}(e^{2i(a_1 \cos(\alpha_1/2)+a_2 \cos\beta)} + e^{-2i(a_1 \cos(\alpha_1/2)+a_2 \cos\beta)})].
\end{aligned} \tag{A.4}$$

Finally:

$$\begin{aligned}
t_{AA}(k) = &2t_3 \cos[2a_1 \sin(\alpha_1/2)k_x] + 2t_7 \cos[2(a_1 \cos(\alpha_1/2) + a_2 \cos\beta] \\
&+ 4\cos[2a_1 \sin(\alpha_1/2)k_x] \cos[2(a_1 \cos(\alpha_1/2) + a_2 \cos\beta)k_y].
\end{aligned} \tag{A.5}$$

A.2 From A to B

The hopping vectors with associated hopping parameters t_1 are:

$$\delta_1^B = -a_1 \sin(\alpha_1/s)\hat{\mathbf{x}} - a_1 \cos(\alpha_1/2)\hat{\mathbf{y}},$$
$$\delta_2^B = a_1 \sin(\alpha_1/s)\hat{\mathbf{x}} - a_1 \cos(\alpha_1/2)\hat{\mathbf{y}}. \tag{A.6}$$

The ones associated with t_4 are:

$$\delta_3^B = -a_1 \sin(\alpha_1/2)\hat{\mathbf{x}} + (a_1 \cos(\alpha_1/2) + 2a_2 \cos\beta)\hat{\mathbf{y}},$$
$$\delta_4^B = a_1 \sin(\alpha_1/2)\hat{\mathbf{x}} + (a_1 \cos(\alpha_1/2) + 2a_2 \cos\beta)\hat{\mathbf{y}}. \tag{A.7}$$

Finally, the ones associated with t_8 are:

$$\delta_5^B = -4a_1 \sin(\alpha_1/2)\hat{\mathbf{x}} - a_1 \cos(\alpha_1/2)\hat{\mathbf{y}},$$
$$\delta_6^B = 4a_1 \sin(\alpha_1/2)\hat{\mathbf{x}} - a_1 \cos(\alpha_1/2)\hat{\mathbf{y}}. \tag{A.8}$$

Therefore, the structure factor $t_{AB}(k)$ is given by:

$$\begin{aligned} t_{AB}(k) = {} & t_1 e^{ia_1 \cos(\alpha_1/2)k_y}\left[e^{ia_1 \sin(\alpha_1/2)k_x} + e^{-ia_1 \sin(\alpha_1/2)k_x}\right] \\ & + t_4 e^{i(a_1 \cos(\alpha_1/2)+2a_2 \cos\beta)k_y}\left[e^{ia_1 \sin(\alpha_1/2)k_x} + e^{-ia_1 \sin(\alpha_1/2)k_x}\right] \\ & + t_8 e^{ia_1 \cos(\alpha_1/2)}\left[e^{4a_1 \sin(\alpha_1/2)k_x} + e^{-4a_1 \sin(\alpha_1/2)k_x}\right]. \end{aligned} \tag{A.9}$$

Finally:

$$\begin{aligned} t_{AB}(k) = {} & 2t_1 e^{-ia_1 \cos(\alpha_1/2)k_y} \cos[a_1 \sin(\alpha_1/2)k_x] \\ & + 2t_4 e^{i(a_1 \cos(\alpha_1/2)+2a_2 \cos\beta)k_y} \cos[a_1 \sin(\alpha_1/2)k_x] \\ & + 2t_8 e^{ia_1 \cos(\alpha_1/2)k_y} \cos[4a_1 \sin(\alpha_1/2)k_x]. \end{aligned} \tag{A.10}$$

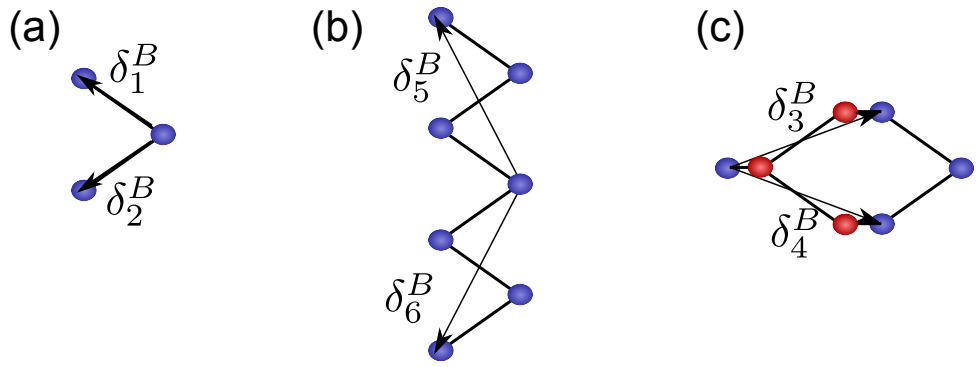

Figure 24: Hopping vectors from an origin site at A to a target site at B.

A.3 From A to C

The hopping vectors associated with t_2 and t_6 are:

$$\delta_1^C = (-2a_1 \cos(\alpha_1/2) - a_2 \cos\beta)\hat{\mathbf{y}},$$
$$\delta_2^C = a_2 \cos\beta\hat{\mathbf{y}}, \tag{A.11}$$

and the ones associated with t_9 are:

$$\delta_3^C = -2a_1 \sin(\alpha_1/2)\hat{\mathbf{x}} - (2a_1 \cos(\alpha_1/2) + a_2 \cos\beta)\hat{\mathbf{y}},$$
$$\delta_4^C = -2a_1 \sin(\alpha_1/2)\hat{\mathbf{x}} + (2a_1 \cos(\alpha_1/2) + a_2 \cos\beta)\hat{\mathbf{y}}. \quad \text{(A.12)}$$

Therefore, the structure factor $t_{AC}(k)$ is given by:

$$t_{AC}(k) = t_6 e^{i(2a_1 \cos(\alpha_1/2)+a_2 \cos\beta)k_y} + t_2 e^{-ia_2 \cos\beta k_y} + t_9 e^{i2a_1 \sin(\alpha_1/2)k_x}[e^{2a_1 \cos(\alpha_1/2)+a_2 \cos\beta)k_y} + e^{-i(2a_1 \cos(\alpha_1/2)+a_2 \cos\beta)k_y}]. \quad \text{(A.13)}$$

And finally:

$$t_{AC}(k) = t_6 e^{i(2a_1 \cos(\alpha_1/2)+a_2 \cos\beta)k_y} + t_2 e^{-ia_2 \cos\beta k_y} + 2t_9 e^{i2a_1 \sin(\alpha_1/2)k_x} \cos[(2a_1 \cos(\alpha_1/2) + a_2 \cos\beta)k_y]. \quad \text{(A.14)}$$

A.4 From A to D

The two vectors associated with t_5 are:

$$\delta_1^D = -a_1 \sin(\alpha_1/2)\hat{\mathbf{x}} - (a_1 \cos(\alpha_1/2) + a_2 \cos\beta)\hat{\mathbf{y}},$$
$$\delta_2^D = a_1 \sin(\alpha_1/2)\hat{\mathbf{x}} - (a_1 \cos(\alpha_1/2) + a_2 \cos\beta)\hat{\mathbf{y}}. \quad \text{(A.15)}$$

Therfore, the structure factor $t_{AD}(k)$ is given by:

$$t_{AD}(k) = t_5[e^{ia_1 \sin(\alpha_1/2)k_x} e^{i(a_1 \cos(\alpha_1/2)+a_2 \cos\beta)k_y} + e^{-ia_1 \sin(\alpha_1/2)k_x} e^{i(a_1 \cos(\alpha_1/2)+a_2 \cos\beta)k_y})$$
$$t_{AD}(k) = 2t_5 e^{i(a_1 \cos(\alpha_1/2)+a_2 \cos\beta)k_y} \cos[a_1 \sin(\alpha_1/2)k_x]. \quad \text{(A.16)}$$

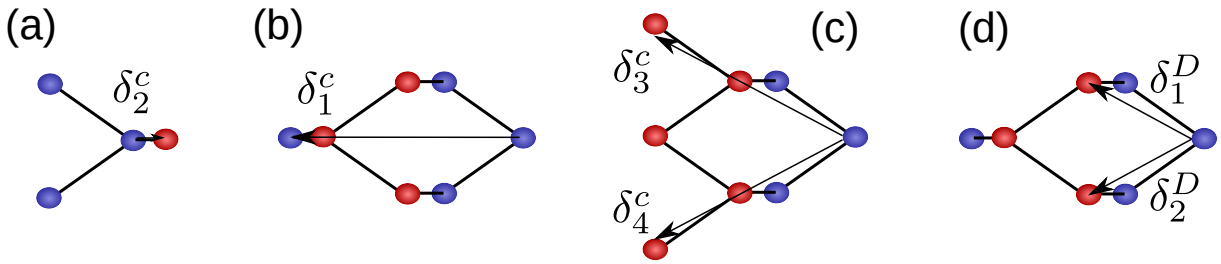

Figure 25: Hopping vectors from an origin site at A to a target site at (a) and (b) C and (c) D.

B SYMMETRY ARGUMENT

The TB monolayer Hamiltonian is given by:

$$H_k = \begin{pmatrix} \epsilon_A + t_{AA}(k) & t_{BA}(k) & t_{DA}(k) & t_{CA}(k) \\ t_{AB}(k) & \epsilon_B + t_{BB}(k) & t_{DB}(k) & t_{CB}(k) \\ t_{AD}(k) & t_{BD}(k) & \epsilon_D + t_{DD}(k) & t_{CD}(k) \\ t_{AC}(k) & t_{BC}(k) & t_{DC}(k) & \epsilon_c + t_{CC}(k) \end{pmatrix} \tag{B.1}$$

Due to the symmetry of phosphorene's crystalline structure, the parameters t_{ik} $(i \neq j)$ can be written in terms of t_{Aj}, where $j = B, C, D$. As seen in Figure, the inversion of the y axis, that is, $y \to -y$ leaves the lattice invariant. This leads to the following relations:

$$\begin{aligned} t_{BD}(k_x, k_y, k_z) &= t_{AC}(k_x, -k_y, k_z) \\ t_{BC}(k_x, k_y, k_z) &= t_{AD}(k_x, -k_y, k_z). \end{aligned} \tag{B.2}$$

Likewise, the inversion of the z axis yields:

$$t_{DC}(k_x, k_y, k_z) = t_{AB}(k_x, k_y, -k_z) \tag{B.3}$$

Since $t_{AC}(k_x, -k_y, k_z) = t^*_{AC}(k_x, k_y, k_z)$,$t^*_{AD}(k) = t^(_{AD}k)$ and $k_z = 0$, we obtain the following relations:

$$\begin{aligned} t_{BD}(k) &= t^*_{AC}(k) \\ t_{BC}(k) &= t_{AD}(k) \\ t_{DC}(k) &= t_{AB}(k). \end{aligned} \tag{B.4}$$

Moreover, $t_{ij} = t^*_{ij}$ for any $i, j = A, B, C, D$. One can also easily show that $t_{AA}(k) = t_{BB}(k) = t_{CC}(k) = t_{DD}(k)$. A pictorial way to visualize this is to "fix" the hopping vectors at an atom at the sublattice A and then "slide" it along the bonds, dragging the hopping vectors along. No matter what sublattice the center from where the hopping vectors stem from, the resulting configuration will be energetically indistin(guishable from the starting point. Therefore, the monolayer Hamiltonian for a given k is given by:

$$H_k = \begin{pmatrix} \epsilon_A + t_{AA}(k) & t^*_{AB}(k) & t_{AD}(k) & t^*_{AC}(k) \\ t_{AB}(k) & \epsilon_B + t_{AA}(k) & t_{AC}(k) & t_{AD}(k) \\ t_{AD}(k) & t^*_{AC}(k) & \epsilon_D + t_{AA}(k) & t^*_{AB}(k) \\ t_{AC}(k) & t_{AD}(k) & t_{AB}(k) & \epsilon_c + t_{AA}(k) \end{pmatrix} \tag{B.5}$$

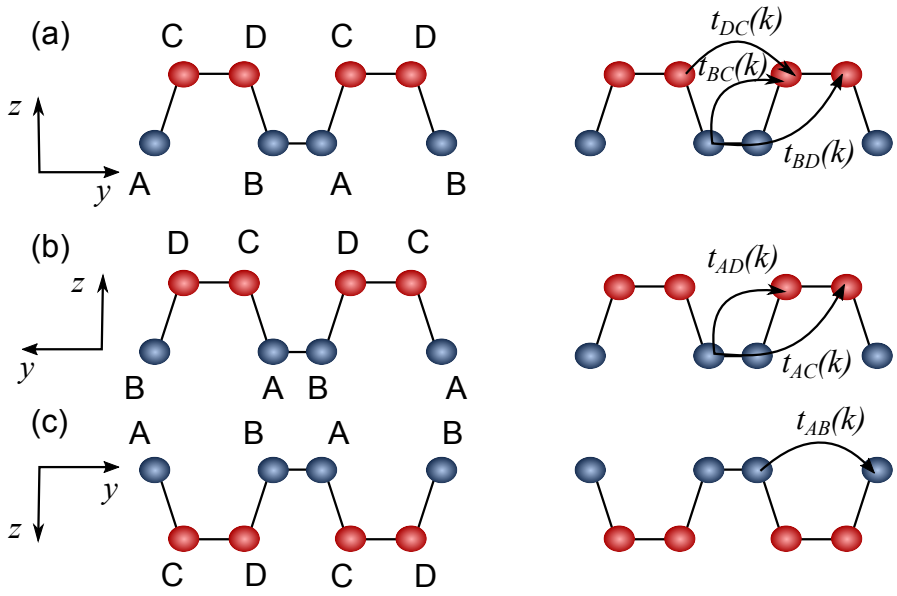

Figure 26: Symmetry of phosphorene sublattices. The structures in (b) and (c) are obtained from the inversions of y and z, respectively, in the structure at (a).

C UNITARY TRANSFORMATION FOR BILAYER BP

In order to obtain the bilayer Hamiltonian, one can apply the following unitary transformation:

$$U = \frac{1}{2}\begin{pmatrix} \mathbf{1} & \mathbf{1} & \mathbf{1} & \mathbf{1} \\ \mathbf{1} & \mathbf{1} & -\mathbf{1} & -\mathbf{1} \\ -i\mathbf{1} & \mathbf{1} & -i\mathbf{1} & \mathbf{1} \\ -i\mathbf{1} & i\mathbf{1} & i\mathbf{1} & -i\mathbf{1} \end{pmatrix}, \tag{C.1}$$

where:

$$\mathbf{1} = \begin{pmatrix} 1 & 0 \\ 0 & 1 \end{pmatrix}. \tag{C.2}$$

Therefore, one obtains:

$$U\mathcal{H}_{bi}U^{\dagger} = \begin{pmatrix} H_0 + H_2 + H_3/2 & 0 & 0 & iH_3/2 \\ 0 & H_0 + H_2 - H_3/2 & -iH_3/2 & 0 \\ 0 & iH_3/2 & H_2 - H_2 - H_3/2 & 0 \\ -iH_3/2 & 0 & 0 & H_0 - H_2 + H_3/2 \end{pmatrix}. \tag{C.3}$$

The secondary diagonal terms can be discarded without significant loss of precision, in accordance with Ref [62]. Therefore, the final bilayer Hamiltonian is:

$$\mathcal{H}'_{bi} = \begin{pmatrix} H_0 + H_2 + H_3/2 & 0 & 0 & 0 \\ 0 & H_0 + H_2 - H_3/2 & 0 & 0 \\ 0 & 0 & H_2 - H_2 - H_3/2 & 0 \\ 0 & 0 & 0 & H_0 - H_2 + H_3/2 \end{pmatrix}. \tag{C.4}$$

REFERENCES

[1] R. B. Jacobs, J. Chem. Phys. **5**, 945 (1937)

[2] P. W. Bridgman, J. Am. Chem. Soc. **36**, 1344 (1914)

[3] X. Ling, H. Wang, S. Huang, F. Xia and M. Dresselhaus. Proc. Nat. Acad. Sci., **112**, 15 (2015)

[4] R. E. Peierls. Ann. I. H. Poincaré **5**, 177-222 (1935)

[5] L. D. Landau. Phys. Z. Sowjetunion **11**, 26-35 (1937)

[6] L. Liao, Y-C. Lin, M. Bao, R. Cheng, J. Bai, Y. Liu, Y. Qu, K. L. Wang, Y. Huang and X. Duan, Nature **467**, 7313 (2010)

[7] R. Hultgren, N. S. Gingrich and B. E. Warren. J. Chem. Phys. **3**, 351 (1935)

[8] L. Li, Y. Yu, G. J. Ye, Q. Ge, X. Ou, H. Wu, D. Feng, X. H. Chen and Y. Zhang. Nat. Nanotechnol. **9**, 5 (2014)

[9] H. Liu, A. Neal, Z. Zhu, Z. Luo, X. Xu, D. Tomanek and P. D. Ye. ACS Nano **8**, 4 (2014)

[10] X. Peng, R. Wei and A. Copple. Phys. Rev. B **90**, 085402 (2014)

[11] A. S. Rodin, A. Carvalho and A. H. Castro Neto. Phys. Rev. Lett. **112**, 176801 (2014)

[12] V. Tran, R. Soklaski, Y. Liang and L. Yang. Phys. Rev. B **89**, 235319 (2014)

[13] R. J. Wu, M. Topsakal, T. Low, M. Robbins, N. Haratipour, J. S. Jeong, R. M. Wentzcovitch, S. J. Koester and K. A. Mkhoyan. J. Vacc. Sci. Tech. A **33**, 060604 (2015)

[14] T. H. Lee, S. Y. Kim and H. W. Jang. Nanomat. **6**, 11 (2016)

[15] J. Guan, W. Song, L. Yang and D. Tomanek. Phys. Rev. B **94**, 045414 (2016)

[16] Q. Wei and X. Peng. Appl. Phys. Lett. **104**, 251915 (2014)

[17] Y. Li, S. Yang and J. Li. J. Phys. Chem. C **118**, 41 (2014)

[18] A. Kistanov, Y. Cai, K. Zhou, S. Dmitriev and Y. Zhang. J. Phys. Chem. C **120**, 12 (2016)

[19] J. Qiao, X. Kong, Z. Hu, F. Yang and W. Ji. Nat. Commun. **5**, 4475 (2014)

[20] M. Sherrott, W. S. Whitney, D. Jariwala, C. M. Went, J. Wong, G. R. Rossman and H. A. Atwater. arXiv:1710.00131v1 [cond-mat.mes-hall]

[21] H. Yuan, X. Liu, F. Afshinmanesh, W. Li, G. Xu, J. Sun, B. Lian, A. G. Curto, G. Ye, Y. Hikita, Z. Shen, S. Zhang, X. Chen, M. Brongersma, H. Y. Hwang and Y. Cui. Nat. Nanotech. **10**, 707-713 (2015)

[22] T. Low, A. S. Rodin, A. Carvalho, Y. Jiang, H. Wang, F. Xia and A. H. Castro Neto. Phys. Rev. B **90**, 075434 (2014)

[23] V. Tran, R. Soklaski, Y. Liang and L. Yang. Phys. Rev. B **89**, 235319 (2014)

[24] X. Wang, A. M. Jones, K. Seyler, V. Tran, Y. Jia, H. Zhao, H. Wang, L. Yan, X. Xu and F. Xia. Nat. Nanotechnol. **10**, 6 (2015)

[25] A. S. Rodin, A. Carvalho and A. H. Castro Neto. Phys. Rev. B **90**, 075429 (2014)

[26] P. Li and I. Applebaum. Phys. Rev. B. **90**, 115439 (2014)

[27] P. W. Bridgman. Proc. Am. Acad. Arts Sci. **76**, 55 (1948)

[28] A. Carvalho, M. Wang, X. Zhu, A. S. Rodin, H. Su and A. H. Castro Neto. Nat. Rev. Mat. **1**, 16061 (2016)

[29] R. W. Keyes. Phys. Rev. **90**, 3 (1953)

[30] A. Brown and S. Rundqvist. Acta. Crystallogr. **19**, 684 (1965)

[31] M. Baba, F. Izumida, Y. Takeda and A. Morita. Jpn. J. Appl. Phys **28**, 6 (1989)

[32] S. Lange, P. Schmidt and T. Nilges. Inorg. Chem. **46**, 4028-4035 (2007)

[33] F. Xia, H. Wang and Y. Jia. Nat. Commun. **5**, 4458 (2014)

[34] S. P. Koenig, R. A. Doganov, H. Schmidt, A. H. Castro Neto and B. Ozyilmaz. Appl. Phys. Lett. **104**, 103106 (2014)

[35] G. Sansone, L. Maschio, D. Usyvat, M. Schtz and A. Karttunen. J. Phys. Chem. Lett. **7**, 131-136 (2015)

[36] J. O. Carlsson and P. M. Martin. *Handbook of Deposition Technologies for Films and Coatings: Science, Applications and Technology.* 3rd ed. Burlington: Elsevier (2010)

[37] J. B. Smith, D. Hagaman and H. F. Ji. Nanothechnology **27**, 215602 (2016)

[38] Z. Cai, B. Liu, X. Zou and H. M. Cheng. Chem. Rev. **118**. 6091-6133 (2018)

[39] J. Pei, X. Gai, J. Yang, X. Wang, Z. Yu, D. Choi, B, Luther-Davies and Y. Lu. Nat. Commun. **7**, 10450 (2016)

[40] V. Nicolosi, M. Chhowala, M. G. Kanatzidis, M. S. Strano and J. N. Coleman. Science **340**, 1226419 (2013)

[41] J. R. Brent, N. Savjani, E. A. Lewis, S. J. Haigh, D. J. Lewis and P. O'Brien. Chem. Comm. **87**, 13338–13341 (2014)

[42] P. Yasaei, B. Kumar, T. Foroozan, C. Wang, M. Asadi, D. Tuschel, J. E. Indacochea, R. F. Klie, A. Salehi-Khojin. Adv. Mat. **27**, 11 (2015)

[43] D. Hanlon, C. Backes, E. Doherty, C. S. Cucinotta, N. C. Berner, C. Boland, K. Lee, A. Harvey, P. Lynch, Z. Gholamvand, S. Zhang, K. Wang, G. Moynihan, A. Pokle, Q. M. Ramasse, N. McEvoy, W. J. Blau, J. Wang, G. Abellan, F. Hauke, A. Hirsch, S. Sanvito, D. D. O'Reagan, G. S. Duesberg, V. Nicolosi and J. N. Coleman. Nat. Commun. **6**, 8563 (2015)

[44] M. Bat-Erdene, M. Batmunkh, C. J. Shearer, S. A. Tawfik, M. J. Ford, L. Yu, A. J. Sibley, A. D. Slattery, J. S. Quinton, C. T. Gibson and J. G. Shapter. Small Methods **1**, 12 (2017)

[45] Z. Yan, X. He, L. She, J. Sun, R. Jiang, H. Xu, F. Shi, Z. Lei and Z. Liu. J. Materiomics **4**, 2 129-134 (2018)

[46] C. R. Ryder, J. D. Wood, S. A. Wells and M. C. Hersma. ACS Nano **10** (4), 3900-17 (2016)

[47] S. L. Yau, T. P. Moffat, A. J. Bard, Z. Zhang and M. M. Lerner. Phys. Rev. Lett.**192**, 383 (1992)

[48] S. Gamage, Z. Li, V. S. Yakovlev, C. Lewis, H. Wang, S. B. Cronin and Y. Abate. Adv. Mat. Interfaces **3**, 1600121 (2016)

[49] A. Favron, E. Gaufres, F. Fossard, A.-L. Phaneuf-Lheureux, N. Y. W. Tang, P. L. Levesque, A. Loiseau, R. Leonelli, S. Francoeur and R. Martel. Nat. Mater. **14**, 826 (2015)

[50] Y. Abate, D. Akinwande, S. Gamage, H. Wang, M. Snure, N. Poudel and S. B. Cronin. Adv. Mater. **30**, 1704749 (2018)

[51] S. Yuan, E. v. Veen, M. I. Katsnelson and R. Roldàn. Phys. Rev. B **93**, 1245433 (2016)

[52] K. Dolui and S. Y. Quek. Scientific Reports **5**, 11699 (2015)

[53] Z. J. Xiang, G. J. Ye, C. Shang, B. Lei, N. Z. Wang, K. S. Yang, D. Y. Liu, F. B. Meng, X. F. Luo, L. J. Zou, Z. Sun, Y. Zhang and X. H. Chen. Phys. Rev. Lett. **115**, 186403 (2015)

[54] R. Fei, V. Tran and L. Yang. Phys. Rev. B **91**, 195319 (2015)

[55] Z. Jiang and Z. Lv. Phys. Lett. A **382**, 3423-3428 (2018)

[56] S. S. Baik, K. S. Kim, Y. Yi and H. J. Choi. Nano. Lett. **15**, 7788-7793 (2015)

[57] J. Kim, S. S. Baik, S. W. Jung, Y. Sohn, S. H. Ryu, H. J. Choi, B. Yag and K. S. Kim. Phys. Rev. Lett. **119**, 226801 (2017)

[58] N. Ehlen, A. Sanna, B. V. Senkovskiy, L. Petaccia, A. V. Fedorov, G. Profeta and A. Gruneis. Phys. Rev. B **97**, 045143 (2018)

[59] C. Dutreix, E. A. Stepanov and M. I. Katsnelson. Phys. Rev. B **93**, 241404 (R) (2016)

[60] A. N. Rudenko, S. Yuan, and M. I. Katsnelson Phys. Rev. B 92, 085419 (2015)

[61] D. J. P. de Sousa, L. V. de Castro, D. R. da Costa, J. M. Pereira, and T. Low Phys. Rev. B 96, 155427 (2017)

[62] J. M. Pereira and M.I. Katsnelson, Phys. Rev. B **92**, 075437 (2015)

[63] L. L. Li, B. Partoens, and F. M. Peeters, Phys. Rev. B **97**, 155424 (2018).

[64] C. W. Groth, M. Wimmer, A. R. Akhmerov and X. Waintal. New J. Phys. **16**,063065 (2014)

[65] K. Wakabayashi, K. Sasaki, T. Nakanishi and T. Enoki, Sci. Technol. Adv. Mater. **11**, 054504 (2010).

[66] L. Brey and H. A. Fertig Phys. Rev. B **73**, 235411 (2006).

[67] A. H. C. Neto, F. Guinea, N. M. Peres, K. S. Novoselov and A. K. Geim. Rev. Mod. Phys. **89**, 109 (2009)

[68] C. W. Groth, M. Wimmer, A. R. Akhmerov and X. Waintal. New J. Phys. **16**,063065 (2014)

[69] K. Wakabayashi, K. Sasaki, T. Nakanishi and T. Enoki, Sci. Technol. Adv. Mater. **11**, 054504 (2010).

[70] D. J. P. de Sousa, L. V. de Castro, D. R. da Costa, and J. M. Pereira, Jr. Phys. Rev. B **94**, 235415 (2016).

[71] A. Carvalho, A.S.Rodin and A. H. Castro Neto, EPL **108**, 47005 (2014)